2017-01-01

Label-Free Raman Imaging to Monitor Breast Tumor Signatures

John Ciubuc
University of Texas at El Paso, inathero@gmail.com

LABEL-FREE RAMAN IMAGING TO MONITOR BREAST TUMOR SIGNATURES

JOHN CIUBUC

Master's Program in Biomedical Engineering

APPROVED:

Felicia Manciu, Ph.D., Chair

Giulio Francia, Ph.D.

Thomas Boland, Ph.D.

Marian Manciu, Ph.D.

Charles Ambler, Ph.D.
Dean of the Graduate School

Dedication

This thesis is dedicated to my beloved parents, Radu Ciubuc and Daniela Ciubuc. I want to thank my parents for their unconditional care and providing me the motivation to achieve my goals. Without their strong support, this work would have been much more difficult to realize.

LABEL-FREE RAMAN IMAGING TO MONITOR BREAST TUMOR SIGNATURES

by

JOHN CIUBUC, B.S.

THESIS

Presented to the Faculty of the Graduate School of

The University of Texas at El Paso

in Partial Fulfillment

of the Requirements

for the Degree of

MASTER OF SCIENCE

BIOMEDICAL ENGINEERING

THE UNIVERSITY OF TEXAS AT EL PASO

MAY 2017

ACKNOWLEDGEMENTS

I'd like to first express my gratitude to my advisor, Dr. Felicia Manciu. Without her support and guidance, I would not be the person that I am today. Dr. Manciu provided the opportunity to take my first steps into the world of research, and with her mentorship, allowed me to achieve my full potential that I would have otherwise been not aware of. Through Dr. Manciu's guidance, I was able to establish a foundation that allowed me to tackle the challenges and hurdles that I encountered, and to successfully overcome them. From the bottom of my heart, I want to thank you for being both the best advisor anyone could have asked for.

I would like to thank Dr. Giulio Francia for his support towards the biological aspect of this project. Dr. Francia always seemed to have the ideal questions to ask and the pointers to provide me the means to answer those questions. With his support, different perspectives revealed themselves to me, allowing me to approach situations in unique ways and generate new outcomes that would have never been possible before.

I would like to thank Dr. Thomas Boland for the immense support that he provided for me throughout my academic adventure in the Biomedical Engineering Master's program. Dr. Boland was always available to assist me with any complications that I encountered, and was always ready to give advice when I needed it. Thank you for making my Biomedical Engineering experience as smooth and stress-free as possible.

Lastly, but certainly not least, I would like to thank Dr. Marian Manciu for the massive support he provided me towards the research and computational side of this thesis. Dr. Manciu introduced me to the world of computational physics and showed me the countless opportunities that were available to me. Thank you for all the support and guidance that you have given me.

I would also like to thank the Granger Foundation and the Research Agreement between the Mayo Clinic at Rochester, Minnesota and the University of Texas at El Paso for making this project a reality.

TABLE OF CONTENTS

LIST OF TABLES

LIST OF FIGURES

LIST OF EQUATIONS

CHAPTER 1: INTRODUCTION

1.1 Breast Cancer Diagnostics

Cancer is a significant disease that has a major impact both in the United States and the rest of the world. With over a million and increasing new cancer cases occurring yearly in the United States, cancer will soon become the number one leading cause of death [1]. Nearly thirty percent of all cancer cases in women alone is attributed to breast cancer [1]. Early, reliable disease detection and diagnosis along with sufficient monitoring post treatment are paramount for increased patient survival with breast cancer. Breast cancer, when detected in its localized stage – stages 0, I, and II, provides the patient with a nearly 100% survival following treatment [2]. Regional breast cancer, stage III, provides a 85% five-year survival rate after treatment [2]. Therefore, enhanced early detection techniques with improved clarity and diagnosis can essentially eradicate the disease that is present in tested individuals.

There are a variety of risk factors that can bring about breast cancer. Familial history of breast cancer along with inherited modifications to the breast cancer attributed genes, such as BRCA1, BRCA2, AKT2, CASP8, MAP3K1, and other related genes can significantly increase risk of breast cancer [3]–[7]. Additionally, age is a contributing factor with a high increase of breast cancer incidence occurring after the age of forty-five [2]. Obesity, dense breast tissue, previous chest radiation, hormone replacement therapy, unnatural levels of estrogen, and consumption of alcohol are other risk factors associated with breast cancer [6], [8]. There is a high difficulty in deriving a method that can prevent breast cancer by simultaneously tackling all the risk factors that can arise to it. Considering the success of breast cancer treatment when targeting early-stage breast cancer, early detection methods are of great importance for defeating breast cancer in its current state.

The majority of breast cancers originate from terminal ductal-lobular units. Mutation of breast epithelial cells within the ducts or lobules form their respective carcinomas (ductal and lobular carcinoma), and are diagnosed as stage 0 breast cancer. Local invasion of the carcinoma denotes stage I breast cancer, with stage II breast cancer being attributed towards larger growth of tumor nodules. Stage III breast cancer is a more progressed form than stage II, in which tumor growths have increased mass from stage II and with regional spread of cancerous cells is observed. Stage IV cancer indicates metastatic breast cancer where the malignant cells have spread to other organs of the body, such as the individual's bones, liver, brain, and lungs.

The current common methods of cancer detection are x-ray mammography, magnetic resonance imaging (MRI), breast ultrasonography, and position emission tomography (PET). Mammography is the most common and widespread method of breast imaging, utilizing low-dose X-rays to exam breast tissue. Whilst mammograms have lowered mortality rates of women by nearly one-third, it is extremely difficult to diagnose early stage breast cancer using this imaging method on account of its high false-positive and false-negative rates [9]–[12]. MRI uses the magnetic properties of the nucleus of hydrogen as its means of imaging. Due to the prevalence of hydrogen in fat, water, and tissues, detailed images for any part of the body can be obtained through MRI, especially when discriminating soft tissue from bone [9]. Regretfully, the limitations of MRI includes slow scanning time, expensive to use, may not clearly make calcifications visible, may lead to several false positives, and certain contrast agents can induce kidney problems or hyperthermia in patients [9], [13]. Breast ultrasonography provides improved cancer detection within denser breast tissue in which mammograms suffer in providing accurate data, yet breast ultrasonography suffers the same issue that breast mammography does regarding its low spatial resolution [14], [15]. PET is a three-dimensional imaging technique that detects γ rays emitted

from external radionuclides that is injected into the body. PET is able to see the differences between normal and cancerous cells based on their metabolic activity [9]. However, PET subjects the patient to high random radiation exposure and it is quite expensive whilst also suffering from poor resolution images [16], [17].

If clarification of the suspect tissue cannot be resolutely confirmed through the sole usage of imaging diagnostics, tissue extraction and analysis is appended to the diagnostic procedures, as seen through histology. Tissue analysis is completed based on the morphological characteristics of the tissue sample, which is due to chemical changes and interactions within the specimen. This analysis brings out accurate observations of the tissue sample, providing a concrete validation if the sample is cancerous or benign. Cancer is a disease that is derived from a multitude of factors in which spectroscopic techniques must be able to discriminate from, thus establishing the different stages of pathogenesis and their underlying mechanisms. Definitive biomarkers came about as a response to this need, thus allowing monitoring of the pathways regarding receptor expression, signal transduction, cellular metabolism and proliferation [9], [18], [19]. Due to the reliance of contrast in analyzing data from images provided by imaging systems, external agents are generally needed for external labeling [20]. External agents focused on these biomarkers help target and increase contrast in these areas of interest thereby providing the suitable environment for imaging systems. However, it would be highly desirable to achieve a method that can provide the sensitivity and specificity of histological analysis, without any labeling agents. This would allow a procedure to have on-site detailed analysis without any specific facilities for tissue extraction, labeling, and analysis. Therefore, having a mechanism for label-free diagnosis is highly desirable and a means to achieving this objective has presented itself: Optical diagnostics.

1.2 Breast Optical Imaging Diagnostics: A Brief History

Advances in medical optical imaging techniques realized a novel idea of utilizing optical techniques for breast cancer diagnosis. In 1929, Dr. Max Cutler suggested that breast tissue may have its own unique optical properties that can differentiate between normal and cancerous cells [21]. Cutler developed a method titled 'transillumination' by which light originating from a powerful emission source penetrates through breast tissue and the projected is observed. The projected image allows for basic visualization of potential lesions, thus giving the observer a rudimentary understanding of the breast's situation. However, complications such as over-illumination, unable to identify deep lesions, and failure to discriminate benign cysts from proper tumors were but a few drawbacks from this technique.

Nearly forty years later, in 1970, technological advances in film and cameras renewed interest in transillumination, which became commonly known as diaphanography techniques. Pulses of visible and near-infrared light are sent through the breast and is registered by a video camera [22]. Multiple different perspectives are used in this diaphanography technique as a means to survey the breast from all possible angles. The obtained data from the video camera is algorithmically transformed and composited to form a desired response. A massive drawback was excessive light scattering resulting in a large amount of light absorption within the breast tissue [22], [23]. The light absorption from the emission source prevented accurate detection of deep lesions. Additionally, due to the visual nature of the technique and reliance on the technical expertise from the operator, this technique was highly prone to error.

A couple decades following the improvements in video camera technology in the early 1990's, the natural progression of technology brought about sophisticated approaches towards optical breast cancer detection. Frequency domain imaging was one major innovation regarding

diaphanography techniques. Frequency domain imaging sought to improve the difficulty diaphanography has in overcoming excess light scattering in breast tissue by utilizing near-infrared light whose properties exhibit enhance penetrance in organic matter. Near-infrared light is highly sensitive towards oxygen attributed species, such as hemoglobin, water, and general oxidation of tissues [24]. Due to significant oxygenation changes coupled with breast tumor formation, near-infrared light became a standard in optical mammography during this period [25], [26].

Taking near-infrared absorption as the foundation for optical mammography, increased focus was directed towards determining the absorption and scattering variables of emitted light through the breast [26]. Frequency domain imaging provided a means of determining a reference to these coefficients by focusing on transmission of photons from narrow-beam transillumination rasterization of the breast tissue utilizing frequency domain algorithms. This method allowed the obtained signal to disregard the photon's path length within the breast, therefore allowing all emitted photons being contributed towards workable data [27]. The obtained signal consists of harmonic components that can be effortlessly decomposed into lower frequency components without any substantial data loss [27]. "Edge-corrected" optical mammograms, commonly known as *N*-images, provide the enhancements in contrast from diaphanography images. The two components derived from frequency domain imaging, the phase and amplitude of the signal, are reconstructed after processing to provide information about breast thickness and oxidation properties. The *N*-image construction algorithm is defined as the following:

$$N(x,y) = \frac{r_0 ac_0}{r(x,y)ac(x,y)}$$

Equation 1.1: *N*-image construction algorithm

Where N is the N-coefficient, x and y indicate the pixel coordinates from image scanning, r_0 defines the separation of plates around the breast, ac_0 is the amplitude where breast is at thickness r_0, $ac(x,y)$ is the amplitude at pixel coordinates and lastly $r(x,y)$ is thickness of breast at pixel that was derived from the phase information. The outcome of this technique allowed for significant improvements regarding discrimination of tumor detection and overall image contrast and quality in comparison to traditional diaphanography [25], [27]. Despite the penetrance properties of near-IR wavelengths in organic tissue, the scattering and absorption of the emission source still has significant influence on both phase and amplitude signals measured from the sample [27]–[29]. As a consequence of this influence, the analysis of the low frequency components may still yield false positive and negative outcomes - higher contrast results are achieved but are not foolproof.

Advancing towards the era of modern breast cancer imaging, tomography has a noteworthy entrance. With near-infrared wavelengths having a growing traction in the field of optical mammography, tomographic systems were able to exhibit their full potential. The average wavelength collection range for topographies are generally between 650 to 830 nm, operating from two to four separate wavelengths. Tomography methods observed concentrations of molecular species from the sample through separation of scattering and absorption coefficients. There is an observable high amount of photon scattering within this range, but the advantages of being sensitive to water, oxy-hemoglobin, deoxy-hemoglobin, and general lipids overcome the initial scattering disadvantage [30]. Tomography methods, enhanced by diffuse approximation, allow visualization of these prominent chromophores and provide detailed characterization and detection of breast cancer. However, limitations of excess scattering, increase in blood attenuation at sub-650 nm wavelengths, and limitations of commercial detectors at above 900 nm cause complications in accuracy regarding signal levels.

Raman spectroscopy is an optical microscopy technique that can potentially remove most of the complications that other techniques exhibit, whilst providing an excellent source of information to analyze data at hand. This technique originated in early 1928, where Sir Chandrasekhara Venkata Raman discovered inelastic scattering, which served as the foundation of the Raman effect. Sir Raman discovered this phenomenon through the crude mechanism of using the sun as his light source and his eyes as his detector. During a sea voyage Sir Raman wanted to discover the reason for the blue color that was emitted by the ocean. Sir Raman could not accept that this blue color was strictly due to the sky's reflection onto the water's surface and so, by procuring a quartz prism from his person, he was able to determine that there was indeed a discrepancy between the color emitted from the water's surface and that from the sky above. Immediately upon returning to his homeland, he went out to recreate this phenomenon and to observe the mechanisms behind this 'molecular diffraction' as Sir Raman labeled it at the time. Through several experiments, purification of numerous solids and liquids and the arrangement of a wide array of different lamp excitation sources, Sir Raman was able to prove and present his findings on 'modified scattering' which later became the technique to bear his name: Raman effect.

Raman scattering gained a huge attraction after its world-wide introduction in the 1930s. the majority of early Raman observations were conducted with the observer's eye as the main detector. The main crux of Raman scattering was the need for improved conditions to observe Raman scattering more easily, due to the nature of only one in ten million photons will exhibit the inelastic scattering that brings about the Raman effect. Therefore, two major areas in Raman spectroscopy sought improvement: the presence of a strong excitation source and improvement of the base sample. A strong excitation source was desired as a means to increase the rate in which Raman scattering occurred. Due to the inherit weakness of the Raman effect, samples were heavily

purified to limit the probability that a Raman signal was attributed to the impurities present in the sample.

1.3 Early Biological Identification and Applications

Raman spectroscopy gives detailed analysis of biological compounds through defined vibrational peaks. Raman's vibrational peaks provide association characteristics to lipids, proteins, nucleic acids, and carbohydrates, giving rise to a fingerprint unique to the particular sample being analyzed. Cancerous and noncancerous cells have discrete morphological characteristics due to chemical composition of their biological constituents. As such, vibrational peaks given by Raman spectroscopy dictate these modifications between the biological compounds and provides different overall spectrums for cancer and noncancerous tissues and cells. Raman spectroscopy has the ability to freely choose excitation wavelengths that avoid water absorption bands, a serious requirement for *in vivo* and living tissue assays. Raman spectroscopy has a clear advantage over other optical spectroscopic techniques by providing real-time direct investigation of biological constituents within a label-free environment.

The advantages of Raman spectroscopy, through its sample chemical composition identification along with water having a minuscule impact on the observed spectrum, naturally lead Raman spectroscopy into the field of biological analysis. Raman spectroscopy has been applied towards plant tissue analytics, mammalian tissue diagnostics, macromolecule breakdowns, molecular bond chemistry, and other biological constituents [31]–[35]. Raman spectroscopy has been considered for usage in medical applications as early as 1988 [36]. Raman spectra obtained from biological materials are quite complex, as the spectra depicts all the biological constituents from the sample in the measured location. Raman spectroscopy entered the field of breast cancer diagnostics in the early 1990's [37].

1.4 Label-Free Raman Spectroscopy in Breast Cancer

Label-free Raman spectroscopy has been used towards breast cancer with great success. The ability to differentiate benign from malignant lesions has been completed in the early 2000's, attaining results of nearly 95% for both sensitivity and specificity in the analysis [38], [39]. Furthermore, profiling of Raman bands through the usage of principal component analysis and multivariant analysis provides a clear distinction between benign and malignant lesions [38]–[40]. However, one important factor to note is that despite benign and malignant discrimination can be effectively done through label-free means, the exact chemical modifications in the observed molecule targets are difficult to discern to the point of being potentially undetectable [38], [40]. *Haka et al.* approached this challenge by developing a macroscopic tissue spectra model for breast tissue. This model provided a reasonably accurate breakdown of biological constituent concentrations in breast cells and tissue, including the cell's nucleus and cytoplasm, collagen, calcium derivatives, and lipid deposits [38]. Other groups also focused on deconvolution of Raman spectra, providing an understanding of present biological constituents, such as lipids, DNA, and proteins, with their related intensities [41].

Despite having a very detailed understanding of macromolecule concentrations and intensities in breast cells, label-free diagnosis of the instigator behind breast cancer has yet to be fully achieved. This is due to biological targets, such as p27, MAPK, and epidermal growth factor receptors, being present in nanomolar concentrations which is below the label-free Raman spectroscopic detection limit [42].

Detection of nanomolar concentrations can be achieved by Raman spectroscopy through the usage of tagging agents. One such method is surface enhanced Raman spectroscopy in which metallic nanoparticles such as gold, silver, quantum dots, and gelatin particles are used in tagging

the desired analytes [43]–[45]. The nanoparticles are developed with specific attachments that show high affinity for the analyte of interest. Once the nanoparticles are distributed in the desired location, activity complexes will form between the nanoparticles and their targets. Plasmon resonance and chemical enhancement can be observed, resulting in an enhancement of the Raman signal [43], [46]. However, surface enhanced Raman spectroscopy is not possible without the usage of tagging agents, and as such it is beyond the scope of this paper.

1.5 Epidermal Growth Factor Receptor Breast Cancer Optical Imaging Targets

Twenty-five to thirty percent of breast cancer is related to HER2/neu oncogene amplification [47]–[49]. HER2 is a member of the transmembrane Epidermal Growth Factor Receptor (EGFR) type I family which also encompasses EGFR(HER1), HER3, and HER4 receptors [50]. EGFR, also known as HER1 and ErbB-1, contains a function intracytoplasmic tyrosine kinase domain and accessible extracellular ligand binding region. EGFR is also responsive to a host of ligands, including EGF, HB-EGF, TGF-α, amphiregulin, epiregulin, betacellulin, and epigen [51]. HER2 lacks an accessible ligand binding region and as such, it is unable to respond to extracellular signals by itself. However, HER2 contains a fully functional tyrosine kinase domain and is able to initiate the signal transduction EGFR pathway. HER3 is the opposite of HER2, where it has no functional tyrosine kinase domain, but has a limited ligand binding region that is responsive towards NRG1 and NRG2 ligands [52], [53]. The final member of the family, HER4, is similar to HER1 in which it has both a tyrosine kinase domain and an accessible ligand binding region, but differs in responding only to neuregulin-class ligands and it is generally present at lower quantities and influence than HER1.

Overexpression of HER1 and HER2 is a prime indicator of carcinogenesis of breast cancer cells due to HER2's special characteristic of always being present in an open dimer configuration

[54]. Despite there being a total of ten different combinations of the dimerization possible within the EGFR family, there's only a small subset within the combinations that actually have biological importance [55]. Within this subset, it is HER2's open dimer configuration that makes it the preferred dimerization partner within the EGFR family, and thus has the most prominent influence [54]. When HER2 creates a dimer complex with another family receptor, HER2 causes a significant amplification of the signal cascade originating from the dimerized receptor. Therefore, in EGFR family related cancer, considering HER1's fully functional and high-influence signal cascade when combined with HER2's signal amplification, overexpression of the heterodimerization of the two receptors gives rise to predominant type of EGFR breast cancer.

The major pathways of interest in EGFR activation are phosphatidylinositol 3-kinase (PI3K) with associated protein kinase B (Akt), mitogen-activated protein kinase (p44/42 MAPK), and a regulator of the cell division cycle, the p27 protein. These pathways are briefly explained in the following subsections. The PI3K/Akt pathway is related to a significant amount of cellular processes including proliferation, differentiation, cell growth, cell survival, and intracellular molecular trafficking. The P13K family has four different classes within, however it is the PIK3CA (p110α) related gene that is found mutated within cancers. This gene codes for a catalytic P13K kinase, in which cancer mutation results in excessive kinase activity. This activity is not exclusive to breast cancer alone, but it is important to note its relationship with EGFR family. EGFR is located directly upstream of the P13K kinase, therefore overexpression of EGFR directly targets and enhances the level of kinase activity from the P13K kinase [56]–[58].

The MAPK/Ras/Raf pathway begins with the activation of EGFR, triggering a phosphorylation event on the intracellular tyrosine kinase domain. The activity in the tyrosine kinase domain causes activation of the guanine nucleotide exchange factor SOS through docking

protein intermediaries, such as GRB2 [59]. SOS activation stimulates GDP removal from GDP-RAS proteins, promoting GTP-RAS formation. The now activated RAS protein (in the form of GTP-RAS) activates RAF kinase, a serine/threonine protein kinase, thereby allowing phosphorylation of MEK1 and MEK2, a pair of serine/tyrosine/threonine kinases [60]. MEK1 and MEK2 can then phosphorylate and activate the mitogen-activated protein kinase MAPK, a serine/threonine protein kinase, which then leads to phosphorylation events of nuclear influencing proteins which result in tumorigenic activity when unregulated [55].

The p27 related pathway is another region of interest due to the cell proliferation regulation ability of p27 itself. The p27 protein serves as a cell proliferation inhibitor by preventing the cell cycle from progressing through the G1 phase into the S phase. Inactivation and degradation of p27 prevents arrest of the G1 phase, therefore allowing the cell to proliferate uncontrollably. Overexpression of the EGFR family accelerates p27 proteolysis due to concomitant pathways inducing p27 polyubiquitination [61]. EGFR can also bind to c-SRC, a non-receptor tyrosine kinase, activating its respective pathway that induces p27 degradation when overexpressed [61]–[63]. EGFR overexpression of Rho- and MAPK-dependent mechanisms can facilitate p27 proteolysis through a Ras intermediary [61], [64]. EGFR amplified pathways may also translocate p27 out from the nucleus and into the cytoplasm [61], [65]. Mislocalization of p27 retains the normal quantity of p27 as seen in non-cancerous cells, yet none of p27's tumor suppressing effects are active [61]. Therapies that target the preservation of p27 have been recorded to cure, or substantially alleviate, EGFR/HER2 amplified cancers [66]–[68].

CHAPTER 2: INTRODUCTION TO SPECTROSCOPIC METHODS

Spectroscopy is the study of the interaction between electromagnetic radiation and matter. Electromagnetic radiation is a form of energy where the properties can be explained in both waves and particles. There are a multitude of techniques that observe these interactions and properties and collect the information into data known as a spectrum, or spectral data. Some of these techniques are Raman Spectroscopy, Fourier transform infrared spectroscopy (FTIR), Mossbauer spectroscopy, atomic absorption spectroscopy (AAS) and X-ray spectroscopy. Each technique obtains spectra information from a different perspective, therefore no single technique is able to provide detailed information of a sample in its entirety. It is common to use a combination of techniques to provide a complete picture, and certain sets complement each other significantly more than other sets. Raman and FTIR is one example of complimenting techniques that provide different perspectives on the same property: vibrational modes of a sample. Raman spectroscopy observes inelastic photon collisions which provides information on symmetrical vibrational modes. FTIR measures interaction between the material and infrared emission, complimenting Raman spectroscopy by giving insights to non-symmetrical vibrational modes.

Materials have unique vibrational modes that formulate a fingerprint identification that is specific to that material alone. In the case of inhomogeneous materials, the constituents have their own unique vibrational modes that can be analyzed as a part of a whole.

2.1 Raman Spectroscopy

Sir Chandrasekhara Venkata Raman discovered a phenomenon with the scattering of light in 1928, which is now known as the Raman Effect. Raman discovered that not all light deflects with a uniform wavelength after encountering a material – instead a small percentage of light will have a change in wavelength after deflection. This change in wavelength is due to the inelastic scattering of photons following deflection. If the incidence photon gives off its energy to the contact material, Stokes Raman scattering occurs. If the opposite is observed, where the material loses energy and the incidence photon gains it upon scattering, this is known as anti-Stokes Raman scattering. The occurrence of inelastic scattering is quite rare, at an average of $\approx 10^{-6}$ photons undergoing the observable effect. However, when there is no modification in wavelength after deflection, elastic scattering occurs which is known as Rayleigh scattering. These observations provided the foundation of Raman spectroscopy.

2.1.1 Classical Description

Consider a molecule that does not have a permanent dipole moment containing a positively charged nucleus that is surrounded by a negatively charged group of electrons. Electromagnetic radiation interacts with the molecule, an oscillating electric field is produced.

The electric field induced by the electromagnetic radiation is as follows:

$$E = E_0 cos(\omega t) = E_0 cos(2\pi\nu_0 t)$$

Equation 2.1: electric field induced by electromagnetic radiation

Where E_0 is the maximum amplitude of the electric field with a dependence on the frequency of the electric field v_0 at time t of incidence of the electromagnetic radiation interaction with the

molecule. The electric field will induce a dipole moment in the molecule which can be described as:

$$\mu = \alpha E = \alpha E_0 cos(\omega_L t)$$

Equation 2.2: Electric field induced dipole moment

Where μ is the dipole moment, α is the polarization of the molecule, E_0 is the maximum amplitude of the electric field with a dependence on ω_L. Molecules generally exhibit asymmetry geometry thereby causing the dipole moment μ to no longer be parallel with electric field E. As such, α is the polarizability tensor of the molecule. The components of the dipole moment μ due to the polarizability tensor α can be written as:

$$\begin{bmatrix} P_x \\ P_y \\ P_z \end{bmatrix} = \begin{bmatrix} \alpha_{xx} & \alpha_{xy} & \alpha_{xz} \\ \alpha_{yx} & \alpha_{yy} & \alpha_{yz} \\ \alpha_{zx} & \alpha_{zy} & \alpha_{zz} \end{bmatrix} \begin{bmatrix} E_x \\ E_y \\ E_z \end{bmatrix}$$

Equation 2.3: Polarizability tensor dipole moment components

The polarization of the molecule is also related to the molecule's vibration. α, being the polarizability tensor, therefore depends on the vibrational coordinate Q, which in return depends on the molecular vibrational angular frequency ω_M, as shown:

$$Q = Q_0 cos(\omega_M t)$$

Equation 2.4: Vibrational coordinate due to molecular vibrational angular frequency

Therefore, the Raman frequency components can be obtained through the amplitude modulation, which is due to the change in polarizability. The variability in polarization can

be easier understood with the implementation of the Taylor series expansion for the polarizability:

$$\alpha = \alpha_0 + \left(\frac{\delta\alpha}{\delta Q}\right)Q + \ldots$$

Equation 2.5: Taylor series expansion for polarizability

Inserting the Taylor series expansion (Eq. 2.5) and the vibrational coordinate *Q* equation (Eq. 2.4) into the induced dipole equation (Eq. 2.2) allows for the following first-order expression to be obtained:

$$\mu = \alpha_0 E_0 \cos(\omega_L t) + \left(\frac{\delta\alpha}{\delta Q}\right) \cdot Q_0 E_0 \cos(\omega_{\mathbf{M}} t) \cdot \cos(\omega_L t)$$

$$\mu = \alpha_0 E_0 \cos(\omega_L t) + \tfrac{1}{2} Q_0 E_0 \left(\tfrac{\delta\alpha}{\delta Q}\right) (\cos((\omega_L - \omega_M) t) + \cos((\omega_L + \omega_M) t))$$

Equation 2.6: First-order induced dipole moment

We can observe three components of the finalized first-order induced dipole moment equation. The first term, [$\alpha_0 E_0 \cos(\omega_L t)$], accounts for no changes in frequency between the scattered light and the incident light, describing what is known as Rayleigh scattering, or elastic scattering. The second term, [$\cos((\omega_L - \omega_M) t)$], accounts for inelastic scattering where the incident photon loses its energy after deflection, also known as Stokes scattering. The third term, [$\cos((\omega_L + \omega_M) t)$], accounts for the other form of inelastic scattering, where the photon gains energy following deflection, and is known as anti-Stokes scattering.

2.1.2 Quantum Approach

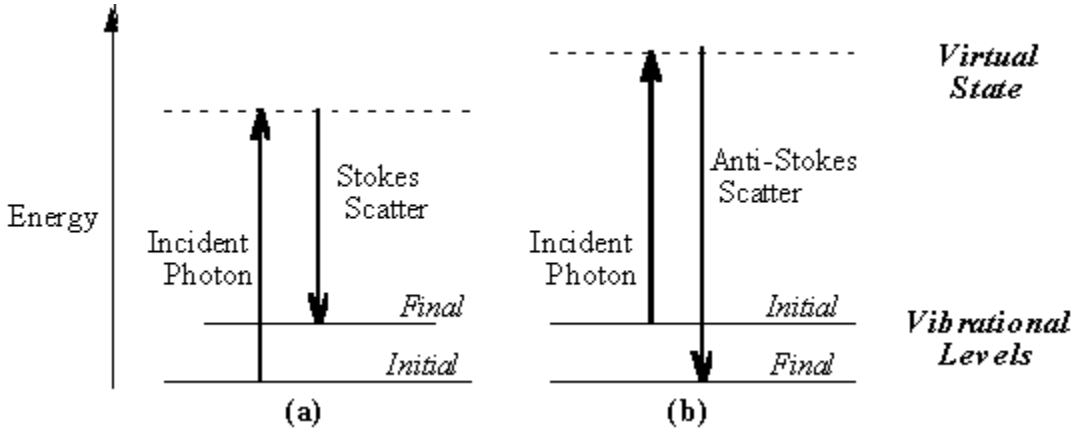

Figure 2.1: Energy level diagram for Raman scattering.
(a) Stokes Raman scattering (b) anti-Stokes Raman scattering [92].

Within a material, there are a multitude of structures available – whether they are simply molecular structures, lattice structures, or general chemical functional groups. A scattered photon that comes within contact of a material's structure will interact with said structure, generally in terms of energy transfer and deflection. During a photon's collision with a structure, a transfer of energy to the structure occurs. This will excite the structure into a virtual quantum state. The structure will return to ground state and re-emit the photon. The re-emitted photon will either have a difference in the energy it had prior to collision, or it will have the same energy from prior to collision. If no changes in energy is observed, the photon's wavelength does not have modification and thus elastic scattering, or Rayleigh scattering, occurs. However, if the structure returns to its ground state and re-emits the photon with less energy from before, the photon will have a change in wavelength, thereby lowering its frequency and increasing its wavelength. This change is miniscule, often within the order of a few wavenumbers (cm^{-1}). If the structure has higher energy than the photon prior to collision, the structure will re-emit the photon with higher

energy, and thus a higher frequency. Observing the spectrum, if the emitted photon has lower energy spectral lines, they are called Stokes spectral lines. In relation, if higher energy spectral lines are observed, they are called Anti-Stokes lines.

2.2 Confocal Raman Spectroscopy

Raman spectroscopy provides several advantages in the world of microscopic analysis from observations obtained from its scattering technique. However, early implementations of the Raman spectroscopic technique suffered slight drawbacks due to its scattering nature. With conventional wide-field microscopy, high resolution imaging was difficult due to the excessive amounts of scattered light. Conventional wide-field microscopy illuminates the entire sample, bringing rise to a numerous amount of scattered light, blurring the overall image. Not only would this cause a blurring in the visual image observed, but this also directly affects the efficacy of the Raman spectroscopic technique applied to the sample. Therefore, a solution was investigated by Professor Marvin Minsky to circumvent this hindrance and provide a new path in high-resolution microscopy [69], [70].

The limitations of wide-field microscopy were overcome in 1957 through Professor Minsky's patenting of confocal imaging. The first steps in confocal microscopy arose with the ideology of focusing on each point of a specimen at a time, instead of viewing the full sample at once. Placement of a small aperture in front of the initial illumination source focuses the illumination onto a singular point upon the sample. Just this small application has the ability to lower the overall amount of scattered light by an appreciable amount whilst improving overall image quality. Whilst this method eliminates the majority of excess light scattering from the illumination source, it does not take in account the excess scattering derived from light reflection off of the sample surface. Elimination of excess surface scattering can be achieved by the

application of a second pinhole aperture located between the image plane and the microscope objective. The second aperture has a secondary effect regarding the manipulation of the depth of field from the sample. In this design, not only is scattered light from out-of-focus points gets discarded, but it also provides the means to obtain a Z-series from the sample. A simplified diagram depicting the process can be observed in Figure 2.2**,** where the optional filters indicate the locations of the pinhole apertures described previously. The quality difference between conventional wide-field microscopy and confocal microscopy can be readily observed in Figure 2.3.

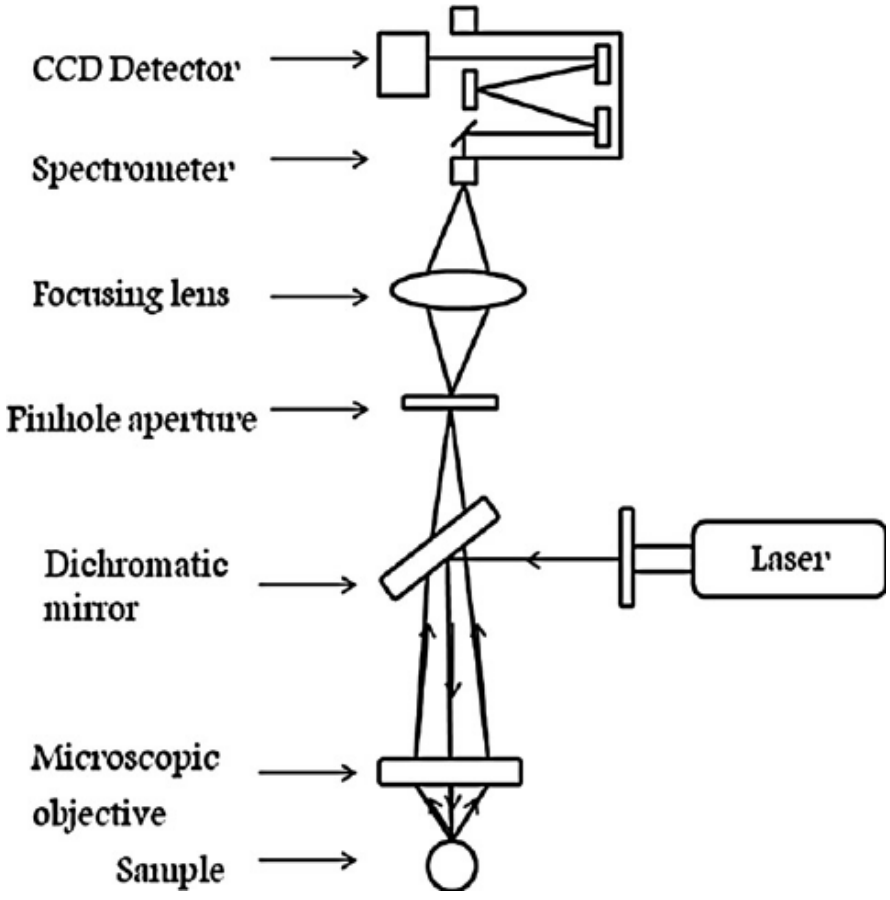

Figure 2.2: Simple Raman confocal microscope diagram
Figure obtained from R. S. Das and Y. K. Agrawal [93].

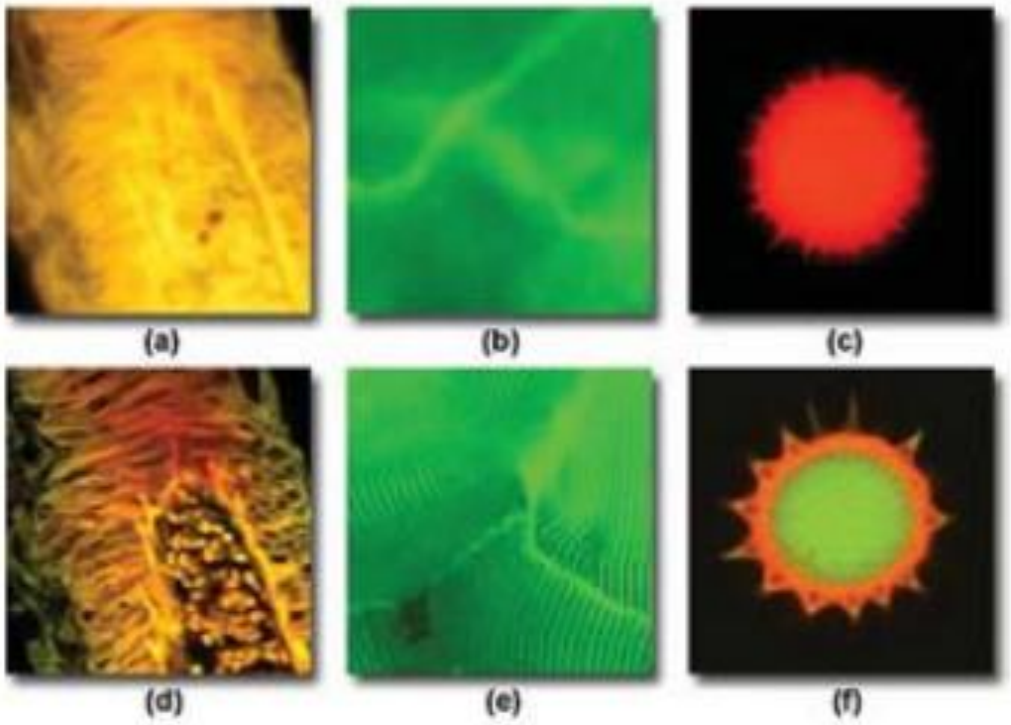

Figure 2.3: Image comparison between wide-field microscopy and confocal microscopy.
(a-c) is attributed towards conventional wide-field microscopy and (d-f) is obtained from confocal microscopy Samples used for comparison are: Human medulla (a, d); Rabbit muscle fibers (b, e); Sunflower pollen grain (c, f) [94].

Confocal microscopy allows for significant improvements in image fidelity, but the very nature of the technique has a draw-back in comparison to wide-field microscopy. Due to the image acquisition being focused on a singular point, an entire mapping of the sample is required to provide a complete image. Initially, when Professor Minsky worked out a method to map the entire sample, it was focused on keeping the laser and microscope instruments stationary whilst moving the stage. This method allowed for a stable and accurate confocal microscopy setup focused on a singular point. Unfortunately, the physical movement of the stage could affect delicate samples, such as organic matter, causing the finalized image to be slightly blurry or misaligned. Advances in confocal microscopy opted for the approach of keeping the sample stage stationary with the

laser having the movable characteristics. A purely stationary sample removed motion induced blurring, but at the cost of more sophisticated optical systems to eliminate potential lens misalignment imperfections.

Raman spectroscopy, when coupled with confocal microscopy, provides excellent data harvesting from a sample. With this system, confocal microscopy provides a point-by-point mapping of the sample in an X-Y-Z data cube model. Each point of this model will have its own unique Raman spectrum associated from it, created at the time of scan integration. The final result is a confocal Raman spectra data set consisting of X-Y-Z data points, where each X-Y pair has its respected Raman spectrum projected in the Z-axis. This data provides excellent visualization of the sample's Raman spectrum in a 3D environment, allowing multiple perspectives and approaches to a sample's Raman spectrum, which is expanded later in Chapter 3.

2.3 Raman Spectrum and Molecular Vibrational Modes

A Raman spectrum is composed of Raman peaks that are dictated by the vibrational modes of a molecule that are derived from the rotational and stretching modes of a molecule. The Raman spectrum consists of a centered point around the wavelength of the initial excitation source, with increasing or decreasing wavenumbers extending from that point as per the experimental setup. The conversion from the observed spectral wavelength to wavenumbers utilized in a Raman spectrum can be observed in the following formula:

$$\Delta\nu = \frac{1}{\lambda_0} - \frac{1}{\lambda_1}$$

Equation 2.7: Wavelength to wavenumber conversion

Where $\Delta\nu$ is the Raman wavenumber converted from spectral wavelength, λ_0 is the excitation wavelength, and λ_0 is the wavelength from the inelastic scattering formed by the Raman effect. When elastic scattering is observed, the values of λ_0 and λ_1 cancel out, providing a net $\Delta\nu$ value of zero, thereby eliminating its contribution to the Raman spectrum. Wavenumbers that follow an increased positivity in value are generated by stokes scattering. Wavenumbers that follow the opposite trend, in which an increase in the negative domain is observed, are generated by anti-stokes scattering. The stokes and anti-stokes Raman peaks that are recorded are red and blue shifted respectively.

The number and intensity of Raman peaks that are observed in a Raman spectrum are always dependent to the number of vibrational modes in a sample. However, not all vibrational modes are represented in the Raman spectrum. This may be due to the vibrational modes not being activated by Raman scattering, or modes exhibiting identical vibrational responses in the presence of the excitation wavelength. Vibrational modes observe a mirror effect around the excitation laser point, where stokes and anti-stokes scattering will exhibit identical displacement from the origin. Additionally, the intensity in Raman peaks formed by anti-stokes scattering will be lower in magnitude in comparison to stokes-scattering, due to the lessened frequency of occurrence.

Vibrational modes in a molecule can be quantified by the measure of atoms within that molecule. By extension, the amount of vibrational modes in a biological sample is reliant on the quantity of its molecular constituents and their respectful atom counts. Molecules are limited by *3N* degrees of freedom, a description bounding the molecule in relation to each of three dimensional Cartesian axes. Furthermore, a molecule is limited in two states, linear or nonlinear, depending on its symmetry around the molecular axis. Therefore, a visualization of each molecule's degree of freedom can be observed in Table 2.1.

Table 2.1. Degrees of Freedom in Linear and Nonlinear Molecules

	Total Degrees of Freedom	Translational Degrees of Freedom	Rotational Degrees of Freedom
Linear Molecules	3N	3	2
Nonlinear Molecules	3N	3	3

The number of atoms present in a molecule is represented by *N*. By obtaining the total degrees of freedom in a molecule, and applying the constraints provided by the translational and rotational degrees of freedom, the remaining degrees of freedom will be the vibrational degrees of freedom. Linear molecules, such as carbon dioxide (O=C=O) and acetylene (H-C≡C-H), have no displacement of nuclei upon rotation around the molecular axis, therefore this rotation is not considered to be a limit of freedom. The formulas for obtaining the vibrational degrees of freedom in linear and non-linear molecules are as follows:

$$\nu_n = 3N - 5$$

Equation 2.8: Degrees of freedom in linear molecules

$$\nu_n = 3N - 6$$

Equation 2.9: Degrees of freedom in non-linear molecules

Where *N* is the quantity of atoms in a molecule and ν_n are the vibrational degrees of freedom. The vibrational degrees of freedom are directly related to the vibrational modes observed as Raman peaks in a Raman spectrum.

2.4 Raman Spectra Analysis

2.4.1 Fluorescence Interference

The background fluorescence that arises during Raman spectroscopy is a huge impediment on the final spectrum. It is important to not confuse fluorescence with Raman scattering, as the difference between the two is quite substantial. Unlike Raman scattering, the incidence photon in fluorescence is completely absorbed by the entire molecule, while it is instead scattered or 'bounced off' in Raman spectroscopy. The absorbed photon in fluorescence increases the overall molecule's energy state to a higher level. The fluorescent photon is then released when the molecule achieves a lower energy state. The fluorescence released lasts over a period of time, several nanoseconds, whereas the scattered photon in Raman scattering occurs instantly.

In highly excitable samples, the fluorescent background can completely eclipse the Raman spectrum, resulting in invalid data. It is important to limit the influence fluorescence interference to expose the underlying Raman spectrum. One particular method of limiting fluorescence is specific selection of the excitation wavelength. Laser excitation wavelengths near infrared (NIR) and ultraviolet (UV) wavelengths tend to show very low to nonexistent fluorescence. The reasoning behind this is twofold. For NIR wavelengths, the excitation photon does not have enough energy for the molecule to exhibit fluorescence. For UV wavelengths, the fluorescence will be far removed from the Raman spectrum itself, therefore no true interference is observed. The drawbacks of far-ranged wavelengths are the limit of sensitivity on detectors. Despite no fluorescence observed, the recorded signal would be negligible in general providing nonvaluable data.

2.4.2 Post-Experimental Fluorescence Elimination

Most fluorescence interference is generally eliminated, or reduced, through post-experimental methods. Background subtraction is the most prominent method, in which the fluorescent background is separated from the Raman spectrum, leaving the resulting Raman spectrum easier to observe. This method takes advantage of the characteristics of fluorescence, where fluorescence exhibits a much larger temporal domain than Raman scattering, and the band response is very broad compared to the Raman band response. By utilizing a high enough polynomial fitting that will account for the changes in fluorescence, a suitable analog to the fluorescence structure can be obtained. Subtraction of the analog from the Raman spectrum will preserve the sharper Raman peaks and eliminate the fluorescence background. Figure 3.1 depicts a before and after example of background subtraction on a Raman spectrum. Specified points depicting fluorescence contributions are selected with orange circles, where a moving polynomial fit is applied as seen in Figure 3.1A. The underlying background that is selected is a similar match to the fluorescent background, and thereby removal of the background results in a clean Raman spectrum as seen in Figure 3.1B.

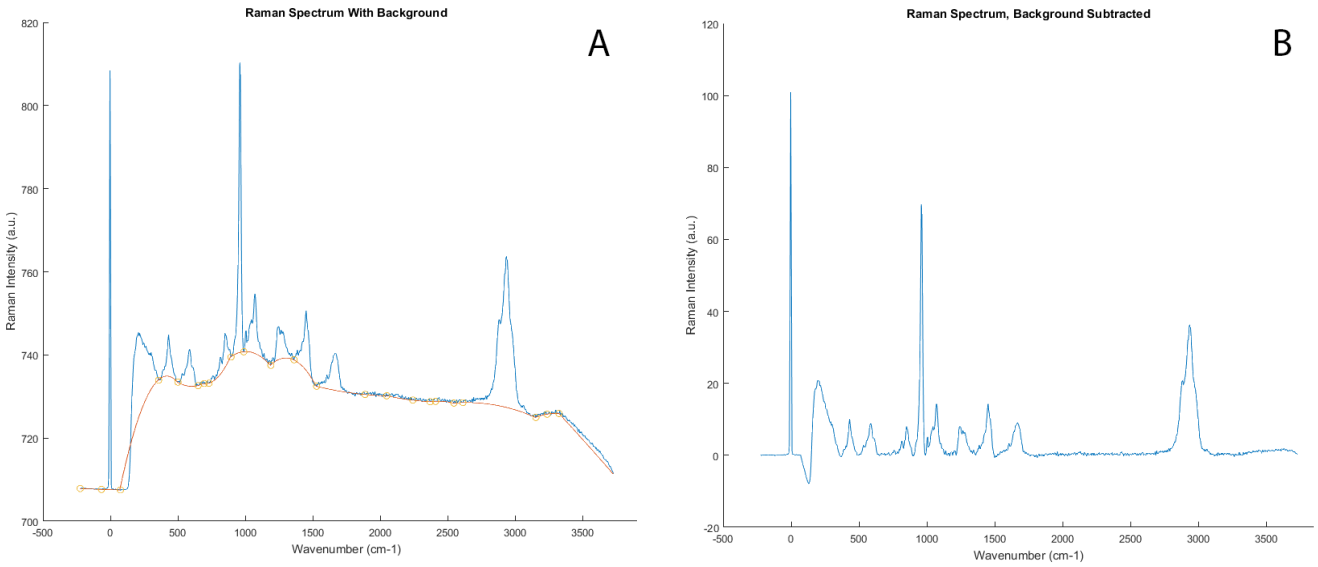

Figure 2.4: Raman spectrum before and after background subtraction

(A) Raman spectrum with fluorescent background. Polynomial background curve indicated in orange. Polynomial discrimination points indicated with orange circles. **(B)** Raman spectrum after background subtraction. Over-prediction subtraction occurred around the 250 cm^{-1} vibration, due to influence of the plasma line. However, this subtraction does not influence the final data, as the low-range wavenumbers are contributed by the fixing agent for this sample.

Another method of background subtraction is the opposite of the previous method, in which the traditional characteristics of Raman peaks are used against the fluorescence background. In this method, the discrimination bias is towards sharper bands resembling Raman responses and against the wider fluorescent bands. Once the pattern recognition is completed, the algorithm can essentially 'pull down' the preserved bands to the baseline, discarding the fluorescent background concurrently.

Aside from polynomial fitting techniques, fast Fourier transforms can also be utilized for background subtraction. Fourier transforming the spectra will provide a frequency domain separation of fluorescence from Raman responses. The lower frequency population will be attributed to the fluorescence response, whereas the higher frequency population will belong to the sharper, Raman responses. A high pass filter can be applied to discard the lower frequency

population whilst retaining the higher frequencies. Application of inverse fast Fourier transform will provide the final Raman spectrum with the fluorescent background absent.

2.5 Raman Spectra Visualization

Raman spectroscopy provides not only a label-free, non-invasive means of molecule identification, but can depict a visual representation of Raman intensity distribution. Confocal Raman microscopy (CRM), a microscopy technique described in the previous chapter, provides the mechanism for Raman spectra visualization. CRM scans over a sample within specified boundaries, obtaining a Raman spectrum for each scanned point. The final series of spectra can be remolded, creating a visualization of both the specimen and the related Raman activity. The advantage of spectra visualization is the ability to observe emergent properties from the visual distribution of Raman activities.

Figure 2.5 shows an example of combining background subtraction and spectra visualization. The sample presented is a low-fluorescent, MCF-7 breast cancer cell, with a focus on the 1240 cm^{-1} band, which is attributed to amide III content in proteins [71]. Figure 2.5A depicts a confocal Raman measurement of the cell without any background subtraction. Despite the cell having low-florescence, the resulting Raman spectra is still quite noisy. Figure 2.5B is the visual spectra after background identification and subtraction is executed. There is a much higher distinction between high activity areas and low activity areas, which was not present before. Through manipulation of exposure values, one can obtain the result in figure 3.2C. In figure 2.5C, the intensity of the amine III vibration is easy to perceive in the MCF-7 cancer cell.

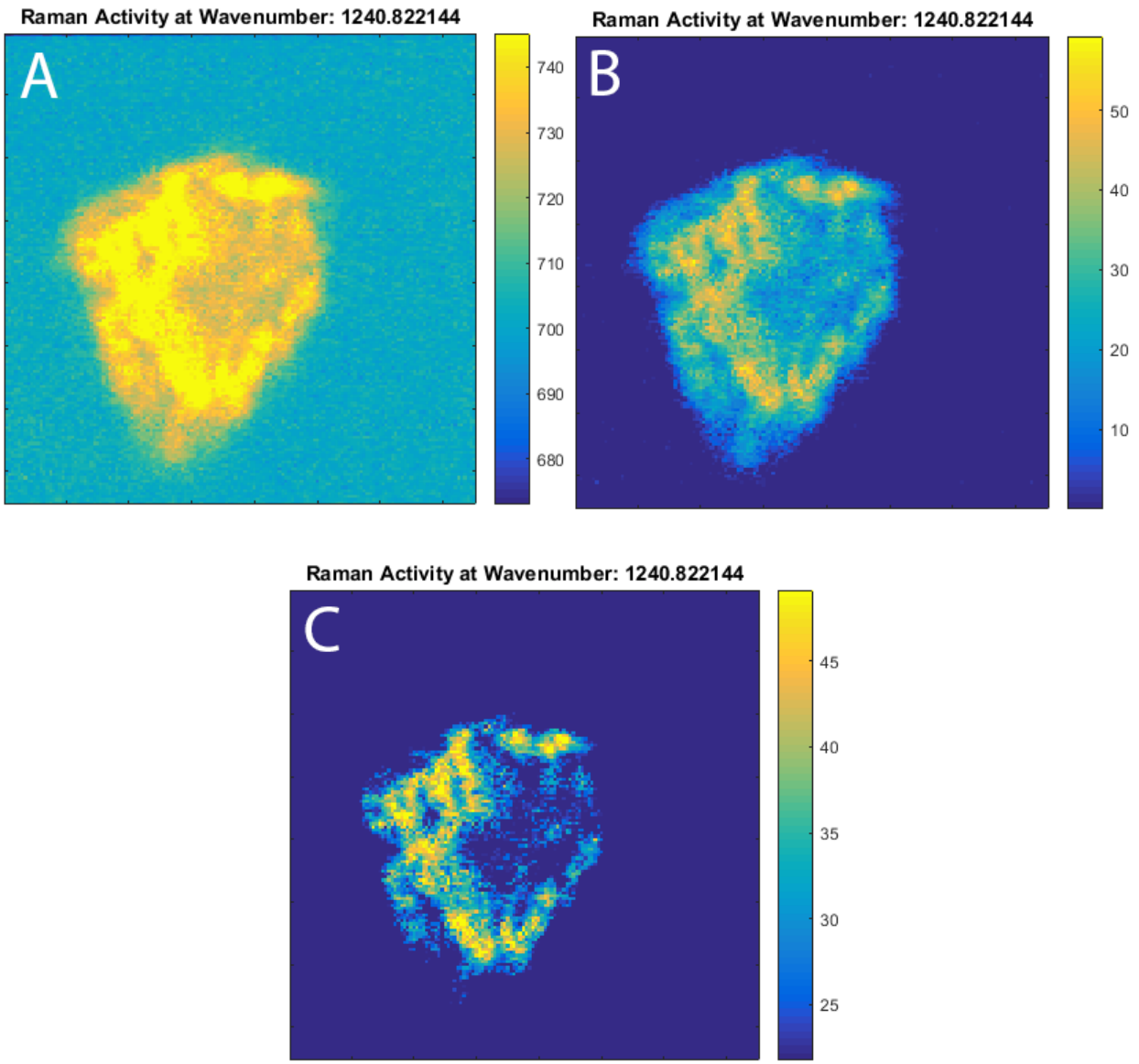

Figure 2.5. Raman background subtraction and spectra visualization on MCF-7 Cancer Cell.

(A) Raman activity visualization of MCF-7 cancer cell at 1240 cm^{-1} band. No background subtraction applied.

(B) Background subtraction applied to original activity spectra. **(C)** Exposure values modified from [B], providing higher distinction of 1240 cm^{-1} band distribution in cell. Visualization and background subtracted was conducted in MATLAB r2016a.

2.5 Experimental Setup

For this study, specific configurations for software, hardware, and cells were used based on the available accommodations.

2.5.1 Control Sample Preparations

MCF-10A (non-tumorigenic breast epithelial cells, control sample) and MCF-7 (tumorigenic, control sample) human breast cancer cell lines were grown under identical conditions in RPMI media, supplemented with 10 % heat-inactivated fetal bovine serum, 100 U/ml penicillin and 100-µg/ml streptomycin. Plain microscope slides coated with Poly-L-lysine were used to grow 500,000 cells over an 8-hour period. After the 8-hour incubation period, cells were washed with 1X PBS- three times and flooded with 4% paraformaldehyde to fix cells for 1 hour at room temperature. After the 1 hour incubation, the samples were again washed three times with 1X PBS and then allowed to air dry for 15 minutes at room temperature.

2.5.2 Western Blotting Configuration

Cells were grown to ~90% confluency in normal culture conditions and starved in serum free media for 24 hours prior to EGF addition. After 24 hours, the control cells were left in serum free media whilst the experimental cells were treated with 100 ng/ml of EGF for 30 minutes. All cells were washed afterwards with ice-cold PBS and detached from plates by trypsin (0.25% wt/v- from Hyclone). Cells were centrifuged for 5 minutes at 1200 rpm. The cell pellets were then resuspended in different cold lysis buffers; RIPA-like [20 mmol/L Tris (pH 7.5) containing 137 mmol/L NaCl, 100 mmol/L NaF, 10% glycerol, 1% NP40, 2 mmol/L Na3VO4, 1 mmol/L phenylmethylsulfonyl fluoride, 10 µg/mL aprotinin, and 10 µg/mL leupeptin], NP-40 [20 mmol/L Tris (pH 8), 137 mmol/L NaCl, 10% glycerol, 1% NP-40, 2mmol/L EDTA], and Milliplex Map Lysis Buffer (Biellerica, MA).

Resuspended cell pellets were then incubated on ice for 10 minutes, and cleared by centrifugation. Protein concentrations of the supernatant were determined using Bio-Rad Protein Assay Dye Reagent (Bio-Rad Laboratories). Samples were resolved on 8-12% SDS-PAGE (30 mg of lysate per lane) and then transferred onto Immobilon-P membranes (Millipore). The membranes were blocked in 10% milk in TBST for 1 h at room temperature. Next, the primary antibodies anti-phospho Akt (Ser473) and anti-phospho p44/42 MAPK (Thr202/Tyr204) (Cell Signaling Technology, Massachusetts-1:1000 dilutions) were added and incubated overnight at 4 °C. membranes were then washed several times in TBST and secondary antibodies (1:5000 dilution) were added for 1 hour at room temperature, and then washed again 5 times in TBST (5 minute per wash) prior to detection using the ECL method (Thermo Fisher).

2.5.3 Confocal Raman Configuration

The confocal Raman measurements were acquired at ambient conditions, in a backscattering geometry, with an alpha300 R WITec system (WITec GmbH, Ulm, Germany) using the 532 nm excitation of a frequency-doubled Nd:YAG laser. Alpha300 R WITec system is shown in Figure 2.6. To avoid sample damage, the laser power was carefully kept at values less than 5 mW. A 488-nm diameter single-mode optical fiber was used to couple the laser beam into the microscope. The laser excitation, filtered by a holographic band-pass filter, was collimated with a 100X objective lens with a numerical aperture (NA) of 0.90 (Olympus, Japan) onto the sample surface. The scattered light collected with the same objective was first passed through a holographic edge filter, and then optically guided using a 50 μm diameter multi-mode optical fiber to a back-illuminated and VIS AR coated Marconi 40-11 CCD detector for data recording. While the single-mode input optical fiber acts as a pinhole source for confocal microscopy, the 50 μm multimode output optical fiber used to couple the collected Raman scattering light to spectrometer functions as an entrance slit. An array of 150 × 150 Raman spectra was recorded for all Raman images using an integration time of 50 ms per spectrum. The surface Raman mapping images of independent cells were acquired with 25 μm × 25 μm scan sizes.

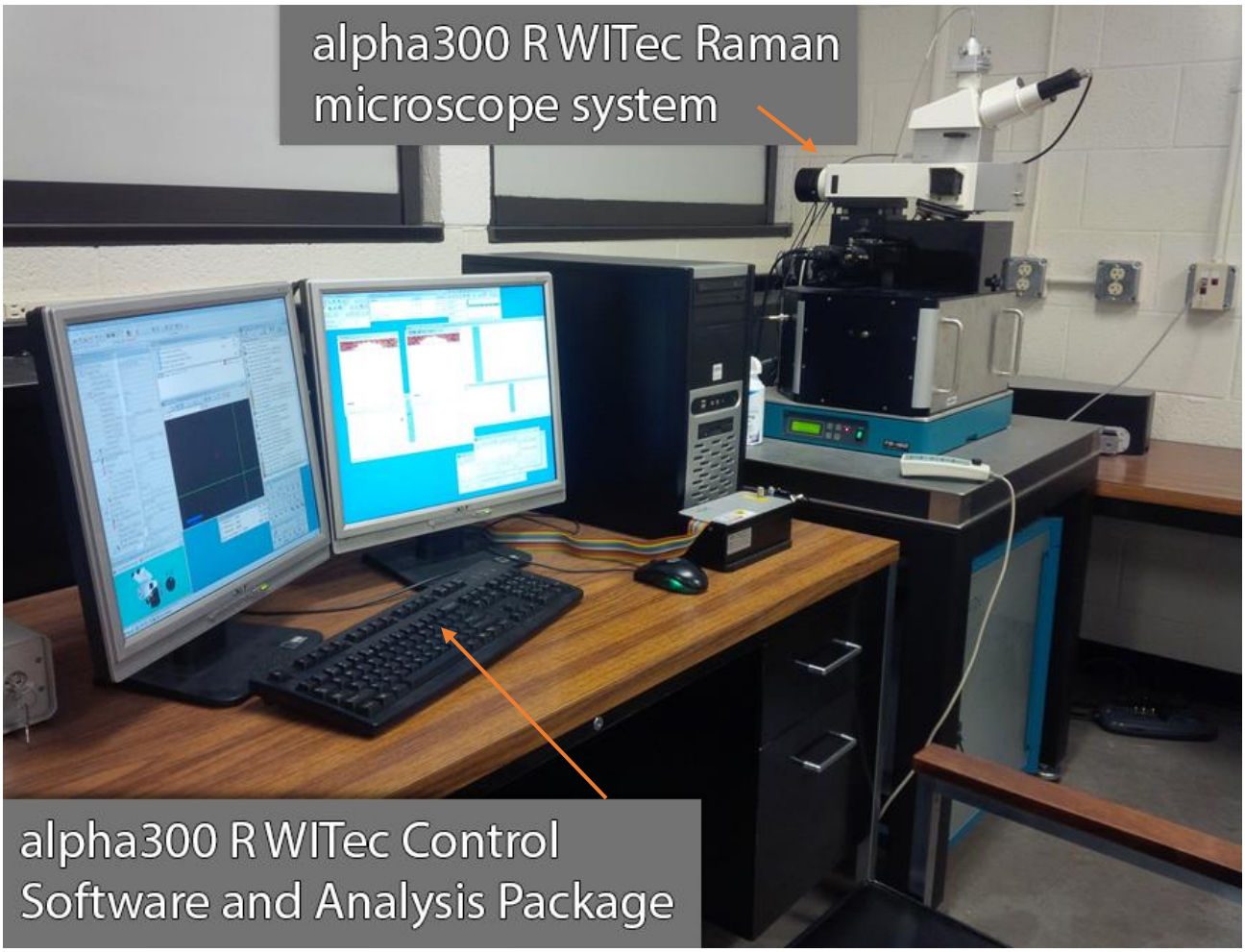

Figure 2.6. Alpha300 R WITec Experimental Setup

The computer system setup with dual displays on the left portion of the figure consists of the alpha300 R WITec Control Software and Analysis Package. The microscope system located above the vibrational-damping leveling platform contains the alpha300 R WITec Raman microscope system.

2.5.3 Data Analysis Configuration

Raman background subtraction and spectral analysis was prototyped in C++11 combined with the Qt cross-platform application framework. Final execution of code was completed in MATLAB R2016a with backwards compatibility that was tested with MATLAB R2013a. WITec's Cluster Analysis package in the WITec Project Plus software accompanied the spectral analysis of the data.

CHAPTER 3: RESULTS AND DISCUSSIONS

3.1 Normal and Cancerous Breast Cell Distinction

With the current implementation of confocal Raman mapping through a raster-scanning technique requiring relatively long acquisition times, several minutes for a complete map, the potential of an *in vivo* application for clinical diagnosis is limited. However, by having a collection of tens of thousands integrated Raman spectra available, it provides an excellent avenue for a more detailed and accurate observation of morphological differences that exist between non-tumorigenic breast epithelial cells and breast cancer cells from a research perspective. Figure 3.1 depicts a visual comparison between the two integrated spectra of non-tumorigenic breast epithelial cells (MCF-10A control sample cells; black line) and breast cancer cells (MCF-7 control sample cells; red line). The comparison of the two integrated spectra show a distinction between the cancerous and non-cancerous indicators through specific intensity variations of vibrational lines, which is in agreement from related reports in literature [72]–[79]. Figure 3.1 contains a break between the 1900 cm^{-1} and 2500 cm^{-1} region, with a slight horizontal axis change following the break for better accentuation and clarification of the areas of interest. The MCF-7 integrated spectrum, as depicted by the red spectrum, was vertically shifted for easier visualization and comparison towards the black, MCF-10A spectrum.

The first important factor to note is the lipid-protein profile that is predominant within the 2800 – 3000 cm^{-1} region. The MCF-7 cancerous spectrum has a significant increase in intensity at the 2940 cm^{-1} Raman peak compared to the noncancerous region, by nearly a factor of two. Contributions of charged amino acids, threonine, histidine, and proline aggregate, forming the observed 2940 cm^{-1} Raman peak. Due to the influence of HER1/2 overexpression, a greater

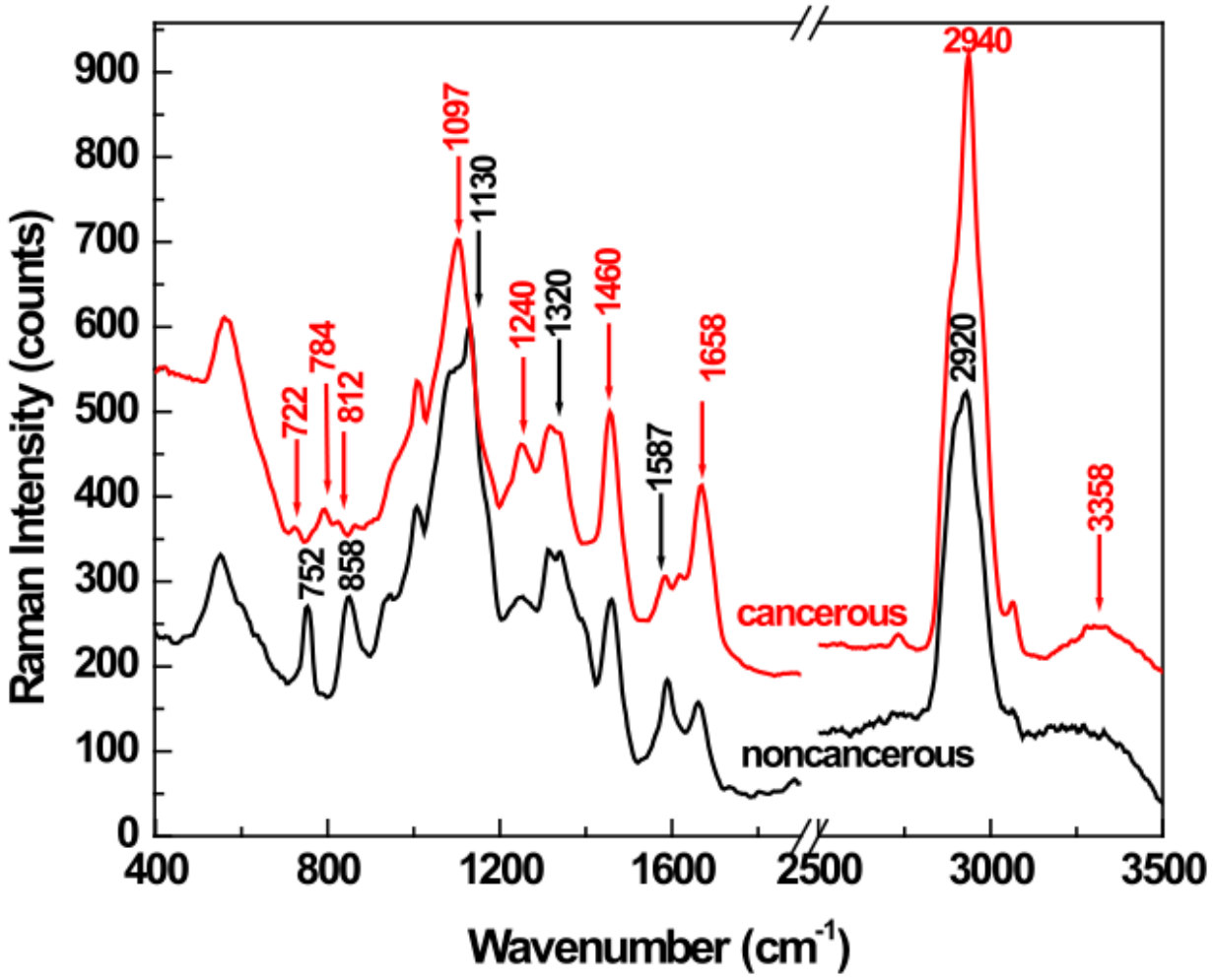

Figure 3.1. Integrated Raman spectra of MCF-10A and MCF-7 confocal Raman mappings

MCF-10A is the non-tumorigenic control sample in the black spectrum. MCF-7 is the breast cancer control sample in the red spectrum. [85]

response is to be expected in the 2940 cm^{-1} Raman peak which has already been considered as one indicator for carcinogenesis [76], [80]. Aromatic and aliphatic groups of amino acids can be located at the 3055 cm^{-1} and 2870 cm^{-1} wavenumbers respectively, where there are no observable differences in the integrated spectra. The broad region located around the 3358 cm^{-1} Raman peak is slightly higher in intensity in the cancerous sample as compared to the noncancerous sample. This region may be associated with the O-H stretching mode present in water [81], however

Raman is known to not be highly sensitive to water absorption therefore this region is more likely to be related to the N-H stretching mode of proteins and N-H stretching mode in DNA's nitrogenous bases [79]. Considering the increase in intensity located at the 1097 cm^{-1} and 1658 cm^{-1} wavenumbers, that are associated with DNA and protein content respectively, the increase in the 3358 cm^{-1} region can be explained due to its relationship with DNA and proteins. Despite the characterization of the 3385 cm^{-1} region is considered to be related with protein and DNA, the potential contribution brought the adipose content within the same region should not be ignored [81].

Following the observed responses of proteins that were briefly mentioned previously, it is important to note the amide modes that are related with protein content and activity. The protein modes in interest are Amide I and III located at 1658 cm^{-1} and 1240 cm^{-1} respectively [71], [82]. The Amide I signature located at 1658 cm^{-1} wavenumber, corresponds to the C=O stretching mode in proteins, and there is a very distinct increase in intensity observed in the cancerous sample in regards to the noncancerous sample. Amide III is located at the 1240 cm^{-1} wavenumber, is related to the C-N stretching and N-H bending modes, where a stark increase in intensity is once again located in the cancerous sample, with only a slight response in the noncancerous sample.

The lower region of the integrated spectra also shows some interesting remarks. The noncancerous region shows a higher intensity response focused on the 752 cm^{-1} and 858 cm^{-1} wavenumbers which are almost not perceptible in the cancerous spectrum. In comparison however, the cancerous spectrum contains a 784 cm^{-1} Raman peak that is absent in the noncancerous spectrum. This change in peaks gives an interesting insight regarding the overall DNA and RNA activity of the cell. The 752 cm^{-1} and 858 cm^{-1} wavenumbers correspond to DNA

nucleic acids and collagen, whereas the 784 cm^{-1} wavenumber relates to both DNA and RNA [71], [73], [82], [83]. This suggests that there is a dramatic reduction in collagen levels in cancerous samples, due to the absence of the 858 cm^{-1} wavenumber, but also a significant modification to DNA and RNA. This remark is further supported by the emergence of a weak 812 cm^{-1} peak in the cancerous sample that corresponds to the PO_2^- stretching mode in RNA [73]. Furthermore, there is a significant influence of the 1097 cm^{-1} peak in the cancerous sample which is associated to the PO_2^- stretching mode of DNA and RNA [73]. Another Raman signature pair can be observed by the 752 cm^{-1} and 1587 cm^{-1} wavenumbers, which are both associated to the ring breathing modes in DNA and RNA [73]. The two wavenumbers have an observable influence in the noncancerous sample, but get severely diminished in the cancerous sample. All the observed signature changes associated to DNA and RNA indicates that there is a significant different in DNA/RNA characteristics between cancerous and noncancerous cells.

In addition to the difference of genetic and protein characteristics, investigations of the cell's surface should not be disregarded. A very weak vibration in the cancerous sample can located at the 722 cm^{-1} wavenumber. This particular vibration is associated to the C-N bond located in the quaternary ammonium groups of sphingomyelins and phosphatidylcholines, two types of lipids that are major components of the cellular membrane [84]. Despite its weak presence, the emergence of this wavenumber implies that there are membrane changes occurring from noncancerous cells to cancerous cells that is associated with sphingomyelins and phosphatidylcholines. Modifications towards these lipids have been reported in literature within the lumen of cancerous breast ducts [74].

The other vibrational lines that depict a Raman response at 600 (broad), 940, 1010, 1320, and 1460 cm^{-1} do not show any noticeable shifting or intensity modifications between the two

samples. The broad band located at the 600 cm^{-1} wavenumber is associated towards paraformaldehyde, which was used for cell fixation. All observed vibrational lines have their assignments provided in Table 3.1 and are additionally marked with red (cancerous) and black (noncancerous) arrows in Figure 3.1.

Table 3.1. Assignments of vibrational modes for the Raman spectra acquired from MCF-7 and MCF-10A cells

Wavenumber (cm^{-1})	Assignment
722	C-N symmetric (membrane phospholipid head) stretching band/nucleotide peak symmetric choline stretch, phospholipids, $(H_3C)N+$ stretch band [86], [87]
752	DNA, nucleic acids, symmetric breathing of tryptophan [75], [87]
784	DNA/RNA, pyrimidine bases of nucleic acids, ring breathing of cytosine [75], [82], [88]
812	PO_2^- stretching mode of RNA [75]
858	C-C stretch proline ring in collagen [82]
1097	DNA, PO_2^- stretching mode [75]
1130	ν(C-C) stretching vibration of lipids from trans-segments and ν(C-N) stretching vibration of proteins [80], [87]
1240	Amide III, collagen [45], [87]
1320	δ(CH) deformation, guanine, CH_3CH_2 wagging nucleic acids, CH_3CH_2 wagging collagen [45], [87]
1460	δ(CH_2, CH_3) asymmetric and symmetric deformations of proteins [45], [82], [87]
1587	Nucleic acids (guanine, adenine), Tryptophan [75], [82], [87]
1658	Amide I in collagen (α-helix), ν(C=O) stretching mode of proteins [75], [82], [87]
2870	ν(CH_2) stretching vibration of lipids [80]
2940	ν(CH_3) asymmetric/symmetric, protein aromatic and aliphatic amino acids [80]
3358	O-H stretching mode of water, N-H stretching vibration of DNA and protein [79], [80], [88]

3.2 EGF Responsive Breast Cell Cancer Distinction

Concluding cancerous and noncancerous breast cell distinction, the dominant indicators of the cellular status is mostly attributed to DNA/RNA and protein characteristics. Considering the overall survival of breast cancer patients following early cancer treatment, accurate detection of both the cancer and the cancer's characteristics could very well make the difference of a patient's outcome. Considering the scenario in which not only cancer detection was established, but the type of cancer is also determined, the patient's survival outlook can approach one-hundred percent survival with targeted therapy. We have considered this by having a qualitative investigation between untreated and treated MCF-7 cancer cells using epidermal growth factor (EGF). EGF is a known cellular proliferation factor that can instigate HER1/2 associated breast cancer. MCF-7 cells were used for this experiment due to their sensitivity and response towards the EGF ligand. In Figure 3.2, we provide a visual mapping of the previous mentioned biological constituents through surface confocal Raman mapping. This provides a high acuity of the location, distribution, and activity of the biological constituents within the cells. Pseudo-coloring was used to provide a visual determination of Raman intensity, where bright yellow indicates high intensity and dark orange indicates low intensity.

Figure 3.2a and 3.2b indicate the accumulation of the nucleic-associated 784 cm^{-1} signature that, not only depicting the cellular nucleic region, but the potential snapshot of the anaphase portion of a cell's division cycle in Figure 3.2a. This observation is given by the

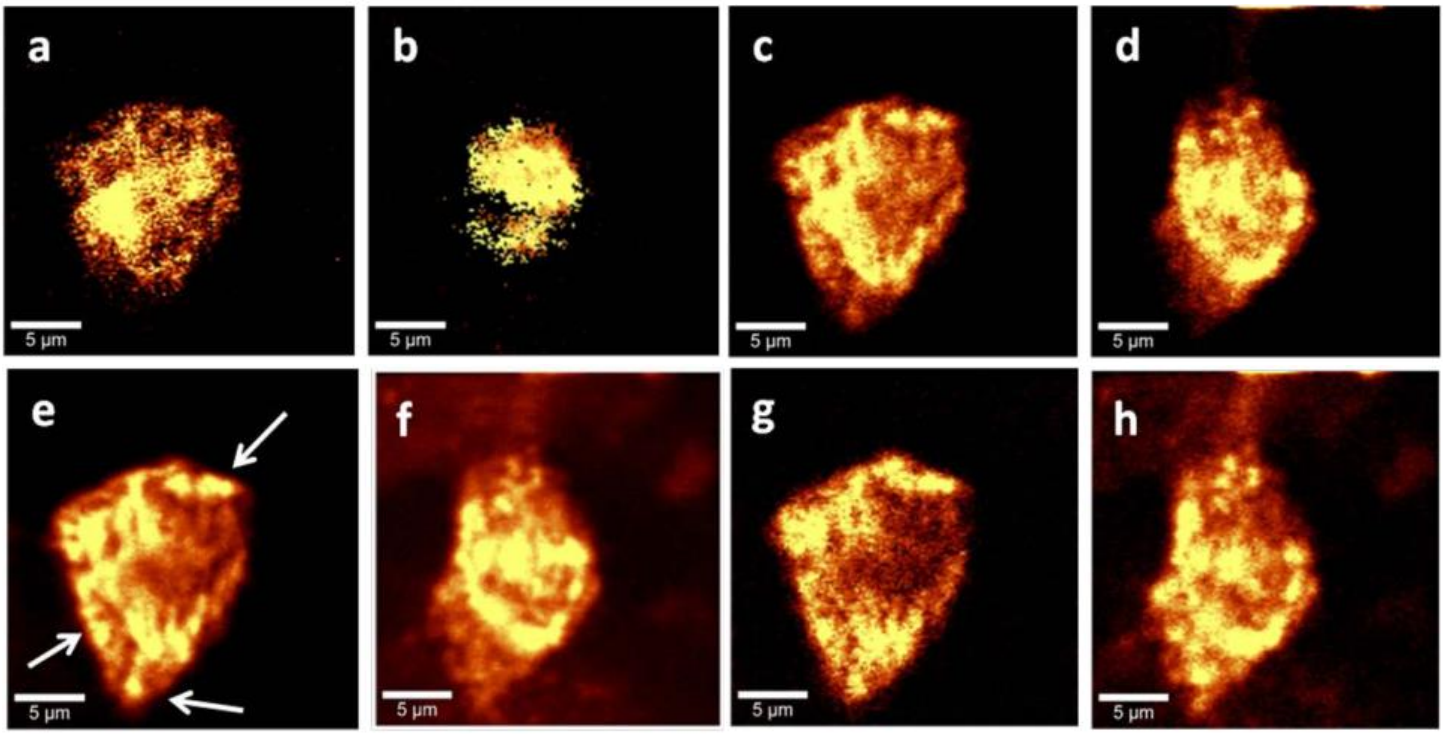

Figure 3.2. Confocal Raman mapping images of vibrational signatures from untreated and EGF-treated MCF-7 Cells

Figures (a, c, e, g) correspond to the untreated MCF-7 cell and Figures (b, d, f, h) correspond to the EGF-treated MCF-7 cell. Figures (a, b) corresponds to DNA/RNA. Figures (c, d) corresponds to the cumulative distribution of 1240 and 1658 cm^{-1} protein signatures. Figures (e, f) corresponds to the 2940 cm^{-1} protein response. Figures (g, h) corresponds to the lipid band feature at 2870 cm^{-1}. Brighter pseudo-colors correspond to higher intensity. Arrows in Figure (e) indicate differences from the presented Figure (c). [85]

observable dual centromeres providing two deposits of high-intensity signatures in the left and right regions of the cell. Figures 3.2c and 3.2d provide the accumulative distribution of the 1240 and 1658 cm^{-1} protein signatures. There were no easily comparable differences between the two images, however the imaging is provided as a comparison point for the next series of mapped Raman features. Figures 3.2e and 3.2f provide a mapping of the 2940 cm^{-1} vibration which looks remarkably similar to the previous set of mappings in figures 3.2c and 3.2d. However, acute observation reveals differences between figures 3.2c and 3.2e, which are marked in the white arrows in figure 3.2e. Focusing on the differences that were revealed, through discrimination

focusing around the 2870 cm^{-1} lipid signature, as depicted in figures 3.2g and 3.2h, confirms the presence marked by the white arrows in figure 3.2e. Through this, we are able to see the rise of a specific lipid-related protein response occurring, which indicates the presence of a close relationship between lipid and protein signatures.

Utilization of advanced background subtraction and enhancing algorithms developed with confocal Raman mapping in mind, we are able to provide single-band enhancement from the Raman mapping data. An alternative to Figures 3.2c-h is provided in Figure 3.3 where the images were conducted through the custom algorithm. Figure 3.3 provides a harsh discrimination of intensity responses, allowing us to not only visually see specifically the highest contributing locations within a cell for that particular band, but also providing a relatively higher resolution snapshot of the cell for that particular. The algorithm used in Figure 3.2 does not allow for such harsh discrimination to occur, but allows an overall picture of the bands in comparison with the rest of the cell's structure. Together, we are given two slightly different perspectives of the same biological constituents present with the cells. Due to the higher discrimination and accentuation of wavenumbers, we are able to observe specific lipid-protein responses in the EGF treated sample that was earlier depicted in the untreated sample. These particular responses are indicated with white arrows in figure 3.3h, showing differences from figures 3.3b and 3.3d.

The importance of cytoplasmic lipid droplets within cancerous cells and tissues has been recently emphasized in literature due to the metabolic resources it provides for the rapidly proliferating cell. It was noted that the altered cellular processes can result in enhanced lipoprotein metabolism that is associated with modified lipogenic enzyme activity throughout all stages of cellular regulation and proliferation [75], [89]. Not only has the generation, and usage,

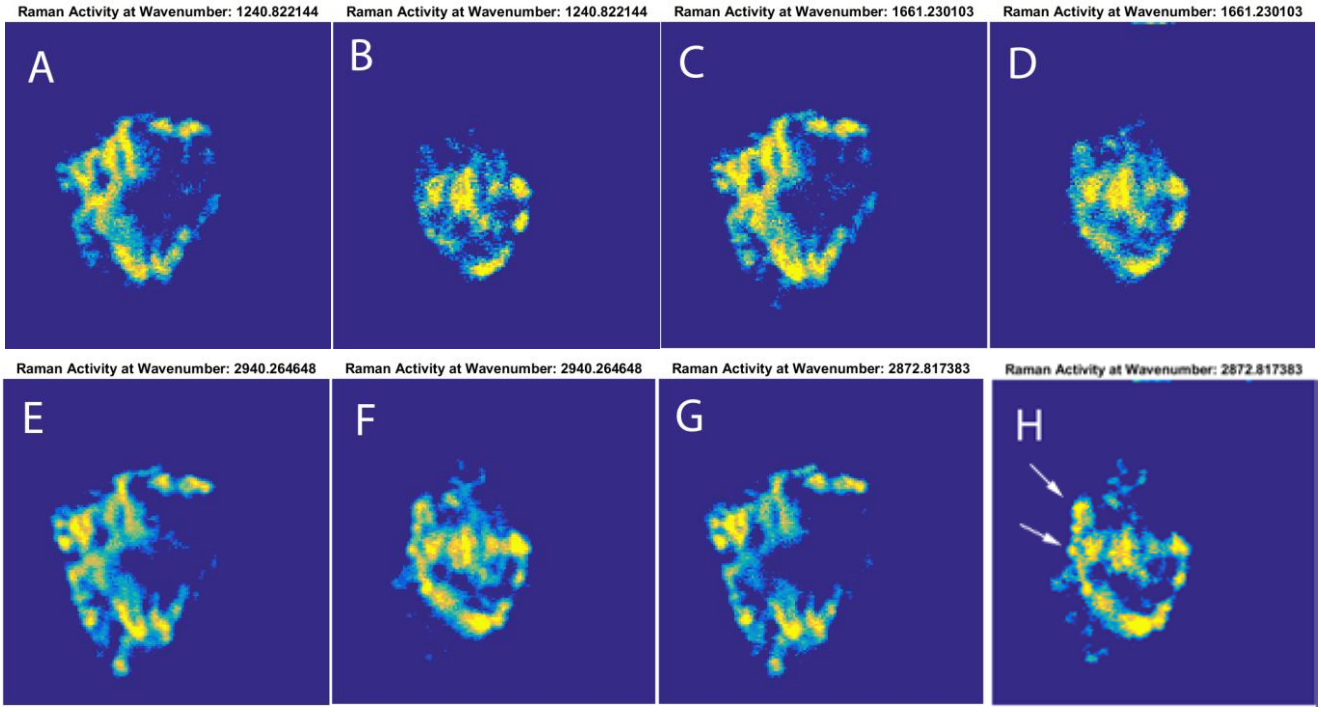

Figure 3.3. In-House algorithmic processing of confocal Raman mapping data of vibrational signatures from untreated and EGF-treated MCF-7 Cells

Figures (a, c, e, g) correspond to the untreated MCF-7 cell and Figures (b, d, f, h) correspond to the EGF-treated MCF-7 cell. Figures (a, b) corresponds to the 1240 cm^{-1} protein signature. Figures (c, d) corresponds to the 1658 cm^{-1} protein signature. Figures (e, f) corresponds to the 2940 cm^{-1} protein response. Figures (g, h) corresponds to the lipid band feature at 2870 cm^{-1}. Brighter pseudo-colors correspond to higher intensity. Arrows in Figure (h) indicate differences presented in Figures (b,c).

of this lipid reservoir been shown to contribute towards cancer proliferation [74], it has also indicated the stimulation of cellular mobility [89]. Figures 3.2g, 3.2h, 3.3f, and 3.3h indicate a good agreement regarding activity of lipid and lipoprotein metabolism, additionally when observing the differences between the untreated and treated MCF-7 cells, with the treated MCF-7 cell having an overall higher expression and intensity of lipid related vibrations. Additionally, this explains the emergence of the 722 cm^{-1} signature as well as the doubling of the 2940 cm^{-1} peak within the cancerous integrated spectrum presented in figure 3.1. Furthermore, as depicted by the white arrows in both figures 3.2 and 3.3, the increase of activity is located closer to the

cell membrane which further emphasizes the contribution of lipid synthesis and metabolism within tumorigenic cell populations.

For better deconstruction and distribution of lower wavenumber associated constituents, those related with DNA/RNA components, the cluster analysis software suite within the WITec Project Plus package was utilized. The cluster mapping data is presented in Figure 3.4a and 3.4b, showing comparative confocal Raman mappings between the untreated and EGF-treated samples. Providing an understanding of spectroscopic data within the micro-scale regions, the graphs presented in figures 3.4c and 3.4d are associated with each cluster with a uniform color coding scheme maintained throughout.

The first comparison to be discussed is the close similarity between figure 3.4a and 3.2a, verifying the accuracy of the calculation regarding DNA/RNA constituents. The second comparison of note is between figures 3.4a and 3.4b, which shows a significant increase of the red region for the EGF-treated cell in comparison to the untreated cell. The increase is rather substantial with the red region of the untreated cell occupying about 20% of the image, whereas a staggering 80% of the treated cell image is occupied by the combined red and green region. The explanation for the treated cell having a green region, instead of being purely red, is due to the discrimination of two specific vibrational responses that was be expanded in more detail later on. To understand why there is such a significant difference in distribution and intensity of DNA/RNA signal, it is crucial to take a detailed look in the provided spectra in figure 3.4c. The dominant feature within the blue spectrum is the 752 cm^{-1} wavenumber. This band steadily decreases within the green spectrum, where the emergence of the 784 cm^{-1} wavenumber contributes to the cluster. In the red spectrum, the 784 cm^{-1} wavenumber reigns dominant with the 752 cm^{-1} peak being mostly extinguished. Throughout this journey, there is an emergence of

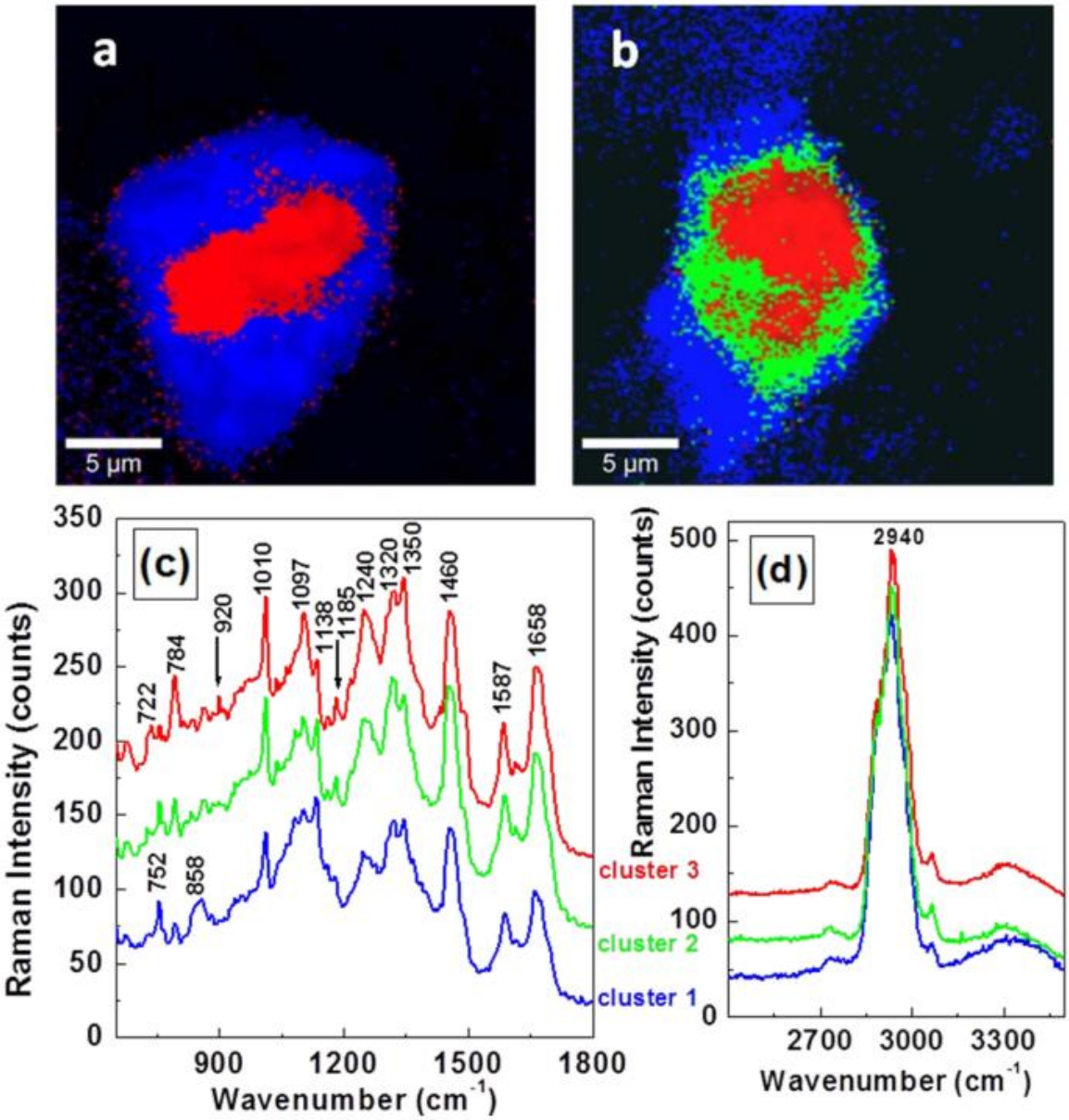

Figure 3.4. Cluster analysis of confocal Raman mapping images from untreated and EGF-treated MCF-7 cells

Figures (a, b) are confocal Raman mapping images processed through the Cluster analysis software in the WITec software analysis suite for untreated and EGF-treated MCF-7 samples respectively. Figures (c, d) correspond to the Raman spectra from each cluster and are focused only in regions of interest. Uniform color code is maintained between all Figures (a, b, c, d). [85]

two completely new peaks, 920 cm^{-1} and 1185 cm^{-1}, which are assigned to phosphorylated threonine and serine respectively [90]. These two wavenumbers are marked with black arrows in

the spectra for greater visibility. The combined emergence of these two wavenumbers suggest the presence of a phosphorylation process that can serve as a means for enhanced proliferation in EGF-treated cells, as evidence by the requirement of threonine and serine site activation for this mechanism [90], [91]. Further validity for this assumption is supported by Western blot analysis which is displayed in figure 3.5. Additionally, a significant decrease of collagen content, as evidenced by the 858 cm^{-1} wavenumber, is seen when traversing from the blue to green to red regions. Furthermore, changes in intensity in the 1320 and 1350 cm^{-1} peaks are observed but there is no particular trend in these changes, besides the slight increase in the 1350 cm^{-1} peak within the red spectrum, suggesting another site of DNA modification. For the protein specific bands located at 1010 cm^{-1}, 1240 cm^{-1}, 1460 cm^{-1}, 1587 cm^{-1}, and 1658 cm^{-1}, no observable intensity changes have occurred. Lastly, the far-wavenumber region of lipids and proteins, the 2800-2900 cm^{-1} region and 2940 cm^{-1} region respectively, also have reports of no observable modifications.

Verification of the EGF activity within the cancer cells was conducted through a Western blot analysis which can be viewed in figure 3.5. The addition of EGF (100 ng/mL) to the MCF-7 cells resulted with the appearance of phosphorylated p44 MAPK (Erk ½ (Thr202/Thr204)) and phosphorylated Akt (Ser473) regardless of the type of lysis buffer employed. The contribution of this data confirms that the presence of the EGF ligand leads to the instigation of several phosphorylation events associated to the known EGF response pathway. With the presence of phosphorylated p44 MAPK and Akt, the Western blot analysis strongly agrees with the emergence of the 920 cm^{-1} and 1185 cm^{-1} peaks within figure 3.4c.

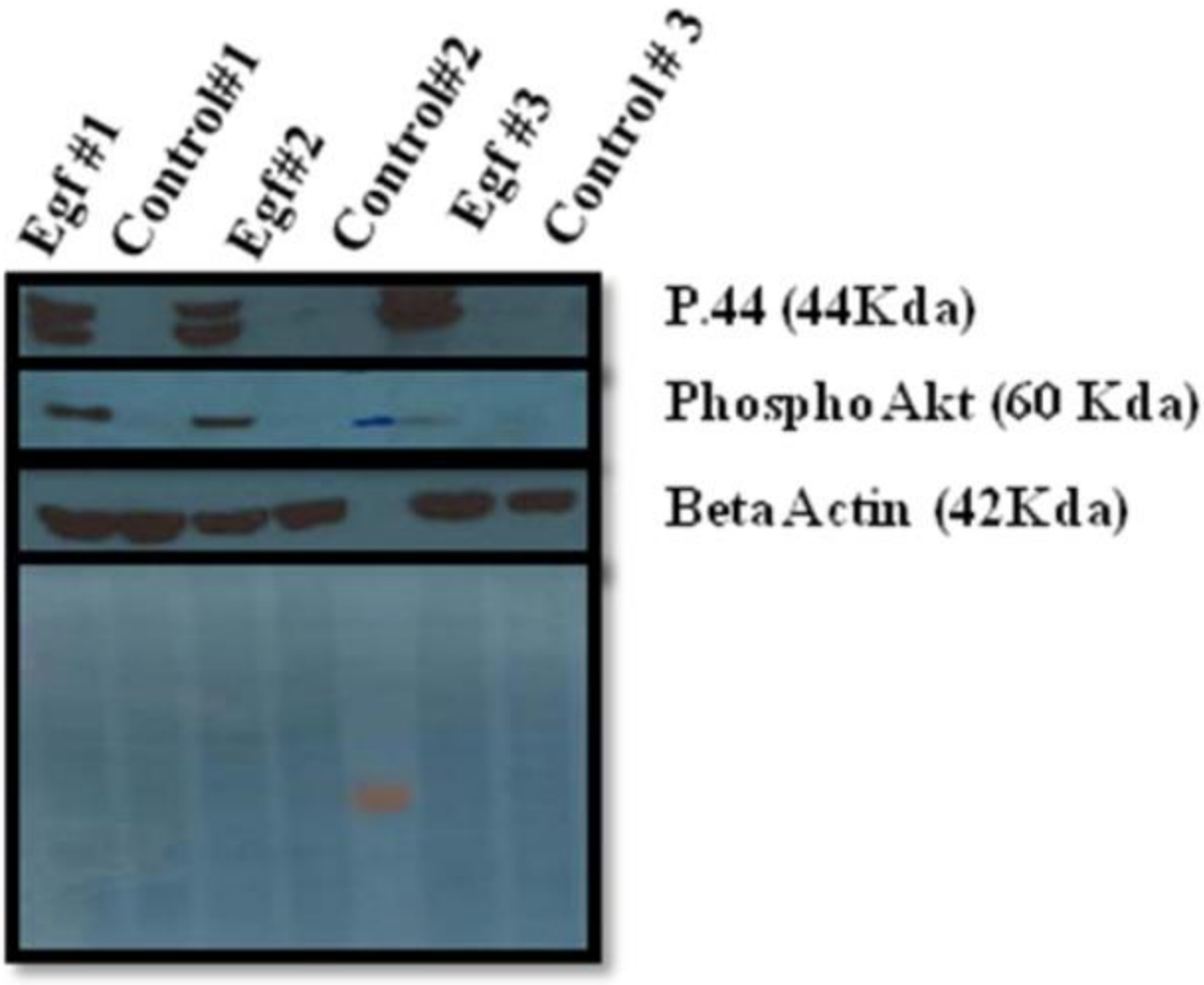

Figure 3.5. Western blotting analysis of EGF stimulation of MCF-7 cells.

The cells were starved for 24 hours prior to EGF exposure for 30 minutes and at a concentration of 100ng/mL, then harvested with 3 different lysis buffers using BD Falcon cell scrapers. The #1 lysis buffer refers to RIPA-like, #2 to NP-40, and #3 to MILLIPLEX MAP for multiplexing. The cells under the control treatment were only treated with RPMI basal media. Amido black staining of the membrane (bottom) indicates even transfer of proteins, and the membrane was probed for phosphorylated p44 MAPK, and phosphor-Akt. Beta-actin was used as an additional loading control. [85]

CHAPTER 4: CONCLUDING REMARKS

Through the utilization of confocal Raman spectroscopy in conjunction with algorithmic methods for data clarification and enhancement, we were able to verify and evaluate EGFR activity in tumor cells through label-free means. Specification of EGF-related activity can provide specific Raman-guided breast tumor diagnosis, that can serve as an advantageous step towards the treatment of this disease. The steps taken in this study confirm that Raman spectroscopy can indeed discriminate tumorous breast cancer cells from nontumorous cells. This data was apparent within the observable modifications and changes that occur in associated DNA/RNA and protein characteristics. However, we decided to ask the following question to ourselves: we are able to determine tumorous from nontumorous cells, but can we also determine tumorous from other tumorous cells? Our steps in answering this question brought us to the comparison of MCF-7 cells instigated by EGF ligands, and MCF-7 cells in the absence of such ligands. The results under these conditions show that we were indeed able to generate distinct Raman profiles depending on the activity of EGF. Not only are modifications observable in the lipid constituents and DNA/RNA contents of the cell, but the emergence of previously unseen vibrations in phosphorylated threonine and serine became apparent. These findings were in good agreement with the following Western blotting analysis results, in which the addition of EGF to MCF-7 cells leads to downstream molecular phosphorylation within the EGFR pathway.

REFERENCES

[1] R. L. Siegel, K. D. Miller, and A. Jemal, "Cancer statistics , 2015 .," *CA Cancer J Clin*, vol. 65, no. 1, p. 29, 2015.

[2] "SEER 18 2008-2012, All Races, Females." [Online]. Available: http://seer.cancer.gov/statfacts/html/all.html. [Accessed: 07-Feb-2016].

[3] M. P. Madigan, R. G. Ziegler, J. Benichou, C. Byrne, and R. N. Hoover, "Proportion of breast cancer cases in the United States explained by well-established risk factors.," *J. Natl. Cancer Inst.*, vol. 87, no. 22, pp. 1681–5, Nov. 1995.

[4] M. C. Pike, D. V Spicer, L. Dahmoush, and M. F. Press, "Estrogens, progestogens, normal breast cell proliferation, and breast cancer risk.," *Epidemiol. Rev.*, vol. 15, no. 1, pp. 17–35, Jan. 1993.

[5] W. D. Dupont and D. L. Page, "Risk factors for breast cancer in women with proliferative breast disease.," *N. Engl. J. Med.*, vol. 312, no. 3, pp. 146–51, Jan. 1985.

[6] K. W. Singletary and S. M. Gapstur, "Alcohol and breast cancer: review of epidemiologic and experimental evidence and potential mechanisms.," *JAMA*, vol. 286, no. 17, pp. 2143–2151, 2001.

[7] P. J. Stephens, P. S. Tarpey, H. Davies, P. Van Loo, C. Greenman, D. C. Wedge, S. N. Zainal, S. Martin, I. Varela, *et al.*, "The landscape of cancer genes and mutational processes in breast cancer," *Nature*, vol. 486, no. 7403, pp. 400–404, May 2012.

[8] Endogenous Hormones Breast Cancer Collaborative Group, E. Hormones, B. Cancer, and C. Group, "Body Mass Index, Serum Sex Hormones, and Breast Cancer Risk in Postmenopausal Women," *JNCI J. Natl. Cancer Inst.*, vol. 95, no. 16, pp. 1218–1226, 2003.

[9] S. V. Sree, "Breast imaging: A survey," *World J. Clin. Oncol.*, vol. 2, no. 4, p. 171, 2011.

[10] N. Obi, A. Waldmann, F. Schäfer, I. Schreer, and A. Katalinic, "Impact of the Quality assured Mamma Diagnostic (QuaMaDi) programme on survival of breast cancer patients," *Cancer Epidemiol.*, vol. 35, no. 3, pp. 286–292,

2011.

[11] R. E. Bird, T. W. Wallace, and B. C. Yankaskas, “Analysis of cancers missed at screening mammography.,” *Radiology*, vol. 184, no. 3, pp. 613–617, 1992.

[12] J. G. Elmore, M. B. Barton, V. M. Moceri, S. Polk, P. J. Arena, and S. W. Fletcher, “Ten-Year Risk of False Positive Screening Mammograms and Clinical Breast Examinations,” *N. Engl. J. Med.*, vol. 338, no. 16, pp. 1089–1096, 1998.

[13] H. T. Le-Petross and M. K. Shetty, “Magnetic Resonance Imaging and Breast Ultrasonography as an Adjunct to Mammographic Screening in High-Risk Patients,” *Semin. Ultrasound, CT MRI*, vol. 32, no. 4, pp. 266–272, 2011.

[14] G. M. Merry and E. B. Mendelson, “Update on Screening Breast Ultrasonography,” *Radiol. Clin. North Am.*, vol. 52, no. 3, pp. 527–537, 2014.

[15] J. Takei, H. Tsunoda-Shimizu, M. Kikuchi, T. Kawasaki, H. Yagata, K. Tsugawa, K. Suzuki, S. Nakamura, and Y. Saida, “Clinical implications of architectural distortion visualized by breast ultrasonography,” *Breast Cancer*, vol. 16, no. 2, pp. 132–135, 2009.

[16] N. Avril and L. P. Adler, “F-18 Fluorodeoxyglucose-Positron Emission Tomography Imaging for Primary Breast Cancer and Loco-Regional Staging,” *Radiol. Clin. North Am.*, vol. 45, no. 4, pp. 645–657, Jul. 2007.

[17] M. C. Abreu, “Clear-PEM: A dedicated pet camera for improved breast cancer detection,” *Radiat. Prot. Dosimetry*, vol. 116, no. 1–4, pp. 208–210, Dec. 2005.

[18] P. a. A. Futreal, L. Coin, M. Marshall, T. Down, T. Hubbard, R. Wooster, N. Rahman, and M. R. M. R. Stratton, “A census of human cancer genes,” *Nat. Rev. Cancer*, vol. 4, no. 3, pp. 177–183, 2004.

[19] H. M. Heneghan, N. Miller, A. J. Lowery, K. J. Sweeney, J. Newell, and M. J. Kerin, “Circulating microRNAs as novel minimally invasive biomarkers for breast cancer.,” *Ann. Surg.*, vol. 251, no. 3, pp. 499–505, 2010.

[20] H. Abramczyk and B. Brozek-Pluska, “Raman imaging in biochemical and biomedical applications. Diagnosis and treatment of breast cancer,” *Chem. Rev.*, vol. 113, no. 8, pp. 5766–5781, 2013.

[21] C. Di Maggio, P. Muzzio, a Di Bello, C. Zacchi, and L. Pescarini, "Transillumination of the breast," *Radiol. Med.*, vol. 62, pp. 401–413, 1976.

[22] A. S. M. Study, "Mammography for the Detection of Breast Cancer in Screening and Clinical Practice," *Cancer*, vol. 65, pp. 1671–1677, 1909.

[23] G. E. Geslien, J. R. Fisher, and C. DeLaney, "Transillumination in breast cancer detection: Screening failures and potential," *Am. J. Roentgenol.*, vol. 144, no. 3, pp. 619–622, 1985.

[24] S. Srinivasan, B. W. Pogue, S. Jiang, H. Dehghani, C. Kogel, S. Soho, J. J. Gibson, T. D. Tosteson, S. P. Poplack, and K. D. Paulsen, "Interpreting hemoglobin and water concentration, oxygen saturation, and scattering measured in vivo by near-infrared breast tomography," *Proc. Natl. Acad. Sci.*, vol. 100, no. 21, pp. 12349–12354, Oct. 2003.

[25] V. E. Pera, E. L. Heffer, H. Siebold, O. Schutz, S. Heywang-Kobrunner, L. Gotz, A. Heinig, and S. Fantini, "Spatial second-derivative image processing: an application to optical mammography to enhance the detection of breast tumors.," *J. Biomed. Opt.*, vol. 8, no. 3, pp. 517–524, 2003.

[26] E. L. Heffer, V. E. Pera, O. Schütz, H. Siebold, and S. Fantini, "Near-infrared imaging of the human breast: complementing hemoglobin concentration maps with oxygenation images.," *J. Biomed. Opt.*, vol. 9, no. 6, pp. 1152–60, 2004.

[27] M. A. Franceschini, K. T. Moesta, S. Fantini, G. Gaida, E. Gratton, H. Jess, W. W. Mantulin, M. Seeber, P. M. Schlag, and M. Kaschke, "Frequency-domain techniques enhance optical mammography: initial clinical results.," *Proc. Natl. Acad. Sci. U. S. A.*, vol. 94, no. 12, pp. 6468–73, 1997.

[28] K. T. Moesta, S. Fantini, H. Jess, S. Totkas, M. A. Franceschini, M. Kaschke, and P. M. Schlag, "Contrast Features of Breast Cancer in Frequency-domain Laser Scanning Mammography," *J. Biomed. Opt.*, vol. 3, no. 2, pp. 129–136, 1998.

[29] P. Taroni, "Diffuse optical imaging and spectroscopy of the breast: A brief outline of history and perspectives," *Photochem. Photobiol. Sci.*, vol. 11, no. 2, p. 241, 2012.

[30] R. Choe, A. Corlu, K. Lee, T. Durduran, S. D. Konecky, M. Grosicka-Koptyra, S. R. Arridge, B. J. Czerniecki, D. L. Fraker, *et al.*, "Diffuse optical

tomography of breast cancer during neoadjuvant chemotherapy: a case study with comparison to MRI.," *Med. Phys.*, vol. 32, no. 4, pp. 1128–39, 2005.

[31] H. J. Butler, L. Ashton, B. Bird, G. Cinque, K. Curtis, J. Dorney, K. Esmonde-White, N. J. Fullwood, B. Gardner, *et al.*, "Using Raman spectroscopy to characterize biological materials," *Nat. Protoc.*, vol. 11, no. 4, pp. 664–687, Mar. 2016.

[32] W. L. Peticolas, "Applications of Raman spectroscopy to biological macromolecules," *Biochimie*, vol. 57, no. 4, pp. 417–428, Jun. 1975.

[33] A. T. Tu, "Use of Raman Spectroscopy in Biological Compounds," *J. Chinese Chem. Soc.*, vol. 50, no. 1, pp. 1–10, Feb. 2003.

[34] M. M. Mariani, P. J. R. Day, and V. Deckert, "Applications of modern micro-Raman spectroscopy for cell analyses," *Integr. Biol.*, vol. 2, no. 2–3, p. 94, 2010.

[35] T. Deckert-Gaudig, E. Kämmer, and V. Deckert, "Tracking of nanoscale structural variations on a single amyloid fibril with tip-enhanced Raman scattering," *J. Biophotonics*, vol. 5, no. 3, pp. 215–219, Mar. 2012.

[36] Y. Ozaki, "Medical Application of Raman Spectroscopy," *Appl. Spectrosc. Rev.*, vol. 24, no. 3–4, pp. 259–312, Sep. 1988.

[37] R. R. ALFANO, C. H. LIU, W. L. SHA, H. R. ZHU, D. L. AKINS, J. CLEARY, R. PRUDENTE, and E. CELLMER, "Human breast tissues studied by IR Fourier transform Raman spectroscopy," *Lasers life Sci.*, vol. 4, no. 1, pp. 23–28.

[38] A. S. Haka, K. E. Shafer-Peltier, M. Fitzmaurice, J. Crowe, R. R. Dasari, and M. S. Feld, "Diagnosing breast cancer by using Raman spectroscopy," *Proc. Natl. Acad. Sci.*, vol. 102, no. 35, pp. 12371–12376, Aug. 2005.

[39] A. S. Haka, Z. Volynskaya, J. A. Gardecki, J. Nazemi, J. Lyons, D. Hicks, M. Fitzmaurice, R. R. Dasari, J. P. Crowe, and M. S. Feld, "In vivo Margin Assessment during Partial Mastectomy Breast Surgery Using Raman Spectroscopy," *Cancer Res.*, vol. 66, no. 6, pp. 3317–3322, Mar. 2006.

[40] J. L. Pichardo-Molina, C. Frausto-Reyes, O. Barbosa-García, R. Huerta-Franco, J. L. González-Trujillo, C. A. Ramírez-Alvarado, G. Gutiérrez-Juárez, and C. Medina-Gutiérrez, "Raman spectroscopy and multivariate

analysis of serum samples from breast cancer patients," *Lasers Med. Sci.*, vol. 22, no. 4, pp. 229–236, Oct. 2007.

[41] S. Rehman, Z. Movasaghi, A. T. Tucker, S. P. Joel, J. A. Darr, A. V. Ruban, and I. U. Rehman, "Raman spectroscopic analysis of breast cancer tissues: identifying differences between normal, invasive ductal carcinoma and ductal carcinomain situ of the breast tissue," *J. Raman Spectrosc.*, vol. 38, no. 10, pp. 1345–1351, Oct. 2007.

[42] T. Dieing, O. Hollricher, and J. Toporski, Eds., *Confocal Raman Microscopy*, vol. 158. Berlin, Heidelberg: Springer Berlin Heidelberg, 2011.

[43] L. J. Lucas, C. Tellez, M. L. Castilho, C. L. D. Lee, M. A. Hupman, L. S. Vieira, I. Ferreira, L. Raniero, and K. C. Hewitt, "Development of a sensitive, stable and EGFR-specific molecular imaging agent for surface enhanced Raman spectroscopy," *J. Raman Spectrosc.*, vol. 46, no. 5, pp. 434–446, May 2015.

[44] E. Chung, J. Lee, J. Yu, S. Lee, J. Hyun, I. Yup, J. Choo, J. H. Kang, I. Y. Chung, and J. Choo, "Use of surface-enhanced Raman scattering to quantify EGFR markers uninhibited by cetuximab antibodies," *Biosens. Bioelectron.*, vol. 60, no. APRIL, pp. 358–365, Oct. 2014.

[45] E. A. Vitol, Z. Orynbayeva, G. Friedman, and Y. Gogotsi, "Nanoprobes for intracellular and single cell surface-enhanced Raman spectroscopy (SERS)," *J. Raman Spectrosc.*, vol. 43, no. 7, pp. 817–827, Jul. 2012.

[46] J. A. Dieringer, A. D. McFarland, N. C. Shah, D. A. Stuart, A. V Whitney, C. R. Yonzon, M. A. Young, X. Zhang, and R. P. Van Duyne, "Introductory Lecture Surface enhanced Raman spectroscopy: new materials, concepts, characterization tools, and applications," *Faraday Discuss.*, vol. 132, pp. 9–26, 2006.

[47] D. J. Slamon, G. M. Clark, S. G. Wong, W. J. Levin, A. Ullrich, W. L. McGuire, A. Biopharma, L. Angeles, D. J. Slamon, *et al.*, "Human breast cancer: correlation of relapse and survival with amplification of the HER-2/neu oncogene.," *Science (80-.).*, vol. 235, no. 4785, pp. 177–182, 1987.

[48] D. J. Slamon, W. Godolphin, L. A. Jones, J. A. Holt, S. G. Wong, D. E. Keith, W. J. Levin, S. G. Stuart, J. Udove, and A. Ullrich, "Studies of the HER-2/neu proto-oncogene in human breast and ovarian cancer.," *Science*, vol. 244, no. 4905, pp. 707–712, 1989.

[49] M. A. Cobleigh, C. L. Vogel, D. Tripathy, N. J. Robert, S. Scholl, L. Fehrenbacher, J. M. Wolter, V. Paton, S. Shak, G. Lieberman, and D. J. Slamon, "Multinational study of the efficacy and safety of humanised anti-HER2 monoclonal antibody in women who have HER2-overexpressing metastatic breast cancer that has progressed after chemotherapy for metastatic disease.," *J Clin Oncol*, vol. 17, no. 9, pp. 2639–2648, 1999.

[50] R. Nahta, D. Yu, M.-C. Hung, G. N. Hortobagyi, and F. J. Esteva, "Mechanisms of Disease: understanding resistance to HER2-targeted therapy in human breast cancer," *Nat. Clin. Pract. Oncol.*, vol. 3, no. 5, pp. 269–280, 2006.

[51] T. P. J. Garrett, N. M. McKern, M. Lou, T. C. Elleman, T. E. Adams, G. O. Lovrecz, H.-J. Zhu, F. Walker, M. J. Frenkel, *et al.*, "Crystal Structure of a Truncated Epidermal Growth Factor Receptor Extracellular Domain Bound to Transforming Growth Factor α," *Cell*, vol. 110, no. 6, pp. 763–773, 2002.

[52] K. L. Carraway III, J. L. Weber, M. J. Unger, J. Ledesma, N. Yu, M. Gassmann, and C. Lai, "Neuregulin-2, a new ligand of ErbB3/ErbB4-receptor tyrosine kinases," *Nature*, vol. 387, no. 6632, pp. 512–516, May 1997.

[53] K. L. Carraway, M. X. Sliwkowski, R. Akita, J. V Platko, P. M. Guy, A. Nuijens, A. J. Diamonti, R. L. Vandlen, L. C. Cantley, and R. A. Cerione, "The Erbb3 Gene-Product Is a Receptor for Heregulin," *J. Biol. Chem.*, vol. 269, no. 19, pp. 14303–14306, 1994.

[54] M. C. Franklin, K. D. Carey, F. F. Vajdos, D. J. Leahy, A. M. De Vos, M. X. Sliwkowski, A. M. De Vos, and M. X. Sliwkowski, "Insights into ErbB signaling from the structure of the ErbB2-pertuzumab complex," *Cancer Cell*, vol. 5, no. 4, pp. 317–328, 2004.

[55] K. Oda, Y. Matsuoka, A. Funahashi, and H. Kitano, "A comprehensive pathway map of epidermal growth factor receptor signaling," *Mol. Syst. Biol.*, vol. 1, no. 1, pp. E1–E17, May 2005.

[56] F. E. Bleeker, S. Lamba, C. Zanon, R. J. Molenaar, T. J. Hulsebos, D. Troost, A. A. van Tilborg, W. P. Vandertop, S. Leenstra, C. J. van Noorden, and A. Bardelli, "Mutational profiling of kinases in glioblastoma," *BMC Cancer*, vol. 14, no. 1, p. 718, Dec. 2014.

[57] F. E. Bleeker, R. J. Molenaar, and S. Leenstra, "Recent advances in the

molecular understanding of glioblastoma," *J. Neurooncol.*, vol. 108, no. 1, pp. 11–27, May 2012.

[58] N. M. Davis, M. Sokolosky, K. Stadelman, S. L. Abrams, M. Libra, S. Candido, F. Nicoletti, J. Polesel, R. Maestro, *et al.*, "Deregulation of the EGFR/PI3K/PTEN/Akt/mTORC1 pathway in breast cancer: possibilities for therapeutic intervention," *Oncotarget*, vol. 5, no. 13, pp. 4603–4650, Jul. 2014.

[59] W. X. Schulze, L. Deng, and M. Mann, "Phosphotyrosine interactome of the ErbB-receptor kinase family," *Mol. Syst. Biol.*, vol. 1, no. 1, pp. E1–E13, May 2005.

[60] J. Avruch, "Ras Activation of the Raf Kinase: Tyrosine Kinase Recruitment of the MAP Kinase Cascade," *Recent Prog. Horm. Res.*, vol. 56, no. 1, pp. 127–156, Jan. 2001.

[61] I. M. Chu, L. Hengst, and J. M. Slingerland, "The Cdk inhibitor p27 in human cancer: prognostic potential and relevance to anticancer therapy.," *Nat. Rev. Cancer*, vol. 8, no. 4, pp. 253–267, 2008.

[62] R. Ishizawar and S. J. Parsons, "C-Src and cooperating partners in human cancer," *Cancer Cell*, vol. 6, no. 3, pp. 209–214, 2004.

[63] M. Grimmler, Y. Wang, T. Mund, Z. Cilenšek, E. M. Keidel, M. B. Waddell, H. Jäkel, M. Kullmann, R. W. Kriwacki, and L. Hengst, "Cdk-Inhibitory Activity and Stability of p27Kip1 Are Directly Regulated by Oncogenic Tyrosine Kinases," *Cell*, vol. 128, no. 2, pp. 269–280, 2007.

[64] J. Liang and J. M. Slingerland, "Multiple Roles of the PI3K/PKB (Akt) Pathway in Cell Cycle Progression," *Cell Cycle*, vol. 2, no. 4, pp. 336–342, 2003.

[65] T. Diabetic and R. Study, "Breast cancer banishes p27 from The nucleus," *Nat. Med.*, vol. 8, no. 9, pp. 8–10, 2002.

[66] F. M. Yakes, W. Chinratanalab, C. A. Ritter, W. King, S. Seelig, and C. L. Arteaga, "Herceptin-induced inhibition of phosphatidylinositol-3 kinase and Akt is required for antibody-mediated effects on p27, cyclin D1, and antitumor action," *Cancer Res.*, vol. 62, no. 14, pp. 4132–4141, 2002.

[67] H. A. Lane, A. B. Motoyama, I. Beuvink, and N. E. Hynes, "Modulation of

p27/Cdk2 complex formation through 4D5-mediated inhibition of HER2 receptor signaling," *Ann. Oncol.*, vol. 12, no. suppl 1, pp. S21–S22, Jan. 2001.

[68] Y. Lu, X. Zi, and M. Pollak, "Molecular mechanisms underlying IGF-I-induced attenuation of the growth-inhibitory activity of trastuzumab (Herceptin) on SKBR3 breast cancer cells," *Int. J. Cancer*, vol. 108, no. 3, pp. 334–341, Jan. 2004.

[69] M. Minsky, "Memoir on inventing the confocal scanning microscope," *Scanning*, vol. 10, no. 4, pp. 128–138, 1988.

[70] S. Inoué, "Foundations of Confocal Scanned Imaging in Light Microscopy," in *Handbook Of Biological Confocal Microscopy*, Boston, MA: Springer US, 2006, pp. 1–19.

[71] R. E. Kast, G. K. Serhatkulu, A. Cao, A. K. Pandya, H. Dai, J. S. Thakur, V. M. Naik, R. Naik, M. D. Klein, G. W. Auner, and R. Rabah, "Raman spectroscopy can differentiate malignant tumors from normal breast tissue and detect early neoplastic changes in a mouse model," *Biopolymers*, vol. 89, no. 3, pp. 235–241, 2008.

[72] K. W. Short, S. Carpenter, J. P. Freyer, and J. R. Mourant, "Raman spectroscopy detects biochemical changes due to proliferation in mammalian cell cultures.," *Biophys. J.*, vol. 88, no. 6, pp. 4274–4288, 2005.

[73] F. Draux, C. Gobinet, J. Sulé-Suso, A. Trussardi, M. Manfait, P. Jeannesson, and G. D. Sockalingum, "Raman spectral imaging of single cancer cells: Probing the impact of sample fixation methods," in *Analytical and Bioanalytical Chemistry*, 2010, vol. 397, no. 7, pp. 2727–2737.

[74] H. Abramczyk and B. Brozek-Pluska, "New look inside human breast ducts with Raman imaging. Raman candidates as diagnostic markers for breast cancer prognosis: Mammaglobin, palmitic acid and sphingomyelin," *Anal. Chim. Acta*, vol. 909, pp. 91–100, 2016.

[75] H. Abramczyk, J. Surmacki, M. Kopeć, A. K. Olejnik, K. Lubecka-Pietruszewska, and K. Fabianowska-Majewska, "The role of lipid droplets and adipocytes in cancer. Raman imaging of cell cultures: MCF10A, MCF7, and MDA-MB-231 compared to adipocytes in cancerous human breast tissue," *Analyst*, vol. 140, no. 7, pp. 2224–2235, 2015.

[76] L. F. Santos, R. Wolthuis, S. Koljenović, R. M. Almeida, and G. J. Puppels, "Fiber-optic probes for in vivo Raman spectroscopy in the high-wavenumber region," *Anal. Chem.*, vol. 77, no. 20, pp. 6747–6752, 2005.

[77] H. Abramczyk, I. Placek, B. Brozek-Pluska, K. Kurczewski, Z. Morawiec, and M. Tazbir, "Human breast tissue cancer diagnosis by Raman spectroscopy," *Spectroscopy*, vol. 22, pp. 113–121, 2008.

[78] K. E. Shafer-Peltier, A. S. Haka, M. Fitzmaurice, J. Crowe, J. Myles, R. R. Dasari, and M. S. Feld, "Raman microspectroscopic model of human breast tissue: implications for breast cancer diagnosisin vivo," *J. Raman Spectrosc.*, vol. 33, no. 7, pp. 552–563, 2002.

[79] C. J. Frank, D. C. Redd, T. S. Gansler, and R. L. McCreery, "Characterization of human breast biopsy specimens with near-IR Raman spectroscopy.," *Anal. Chem.*, vol. 66, no. 3, pp. 319–326, 1994.

[80] H. Abramczyk, J. Surmacki, B. Brozek-Płuska, Z. Morawiec, and M. Tazbir, "The hallmarks of breast cancer by Raman spectroscopy," *J. Mol. Struct.*, vol. 924–926, no. C, pp. 175–182, 2009.

[81] H. Abramczyk, B. Brozek-Pluska, M. Krzesniak, M. Kopec, and A. Morawiec-Sztandera, "The cellular environment of cancerous human tissue. Interfacial and dangling water as a 'hydration fingerprint,'" in *Spectrochimica Acta - Part A: Molecular and Biomolecular Spectroscopy*, 2014, vol. 129, pp. 609–623.

[82] G. R. Lloyd, L. E. Orr, J. Christie-Brown, K. McCarthy, S. Rose, M. Thomas, and N. Stone, "Discrimination between benign, primary and secondary malignancies in lymph nodes from the head and neck utilising Raman spectroscopy and multivariate analysis," *Analyst*, vol. 138, no. 14, pp. 3900–3908, 2013.

[83] A. Saha, I. Barman, N. C. Dingari, S. McGee, Z. Volynskaya, L. H. Galindo, W. Liu, D. Plecha, N. Klein, R. R. Dasari, and M. Fitzmaurice, "Raman spectroscopy: a real-time tool for identifying microcalcifications during stereotactic breast core needle biopsies," *Biomed. Opt. Express*, vol. 2, no. 6, p. 2792, 2011.

[84] S. Uskoković-Marković, M. Jelikić-Stankov, I. Holclajtner-Antunović, and P. Đurđević, "Raman Spectroscopy as a New Biochemical Diagnostic Tool," *J. Med. Biochem.*, vol. 32, no. 2, pp. 96–103, 2013.

[85] F. S. Manciu, J. D. Ciubuc, K. Parra, M. Manciu, K. E. Bennet, P. Valenzuela, E. M. Sundin, W. G. Durrer, L. Reza, and G. Francia, "Label-Free Raman Imaging to Monitor Breast Tumor Signatures.," *Technol. Cancer Res. Treat.*, 2016.

[86] J. G. Paez, P. A. Jänne, J. C. Lee, S. Tracy, H. Greulich, S. Gabriel, P. Herman, F. J. Kaye, N. Lindeman, *et al.*, "EGFR mutations in lung cancer: correlation with clinical response to gefitinib therapy.," *Science*, vol. 304, no. 5676, pp. 1497–500, 2004.

[87] J. Kneipp, T. Bakker Schut, M. Kliffen, M. Menke-Pluijmers, and G. Puppels, "Characterization of breast duct epithelia: A Raman spectroscopic study," in *Vibrational Spectroscopy*, 2003, vol. 32, no. 1 SPEC., pp. 67–74.

[88] M. V. P. Chowdary, K. K. Kumar, J. Kurien, S. Mathew, and C. M. Krishna, "Discrimination of Normal, Benign, and Malignant Breast Tissues by Raman Spectroscopy," *Biopolymers*, vol. 83, no. 5, pp. 556–569, 2006.

[89] C. J. Antalis, A. Uchida, K. K. Buhman, and R. A. Siddiqui, "Migration of MDA-MB-231 breast cancer cells depends on the availability of exogenous lipids and cholesterol esterification," *Clin. Exp. Metastasis*, vol. 28, no. 8, pp. 733–741, 2011.

[90] L. Ashton, C. Johannessen, and R. Goodacre, "The importance of protonation in the investigation of protein phosphorylation using raman spectroscopy and raman optical activity," *Anal. Chem.*, vol. 83, no. 20, pp. 7978–7983, 2011.

[91] N. Kumar, R. Afeyan, S. Sheppard, B. Harms, and D. A. Lauffenburger, "Quantitative analysis of Akt phosphorylation and activity in response to EGF and insulin treatment," *Biochem. Biophys. Res. Commun.*, vol. 354, no. 1, pp. 14–20, 2007.

[92] "Raman Spectroscopy - A Tutorial." [Online]. Available: http://www.kosi.com/na_en/products/raman-spectroscopy/raman-technical-resources/raman-tutorial.php. [Accessed: 20-Feb-2016].

[93] R. S. Das and Y. K. Agrawal, "Raman spectroscopy: Recent advancements, techniques and applications," *Vib. Spectrosc.*, vol. 57, no. 2, pp. 163–176, 2011.

[94] T. Fellers and M. Davidson, "Olympus Microscopy Resource Center | Confocal Microscopy - Introduction." [Online]. Available:

http://olympus.magnet.fsu.edu/primer/techniques/confocal/confocalintro.html. [Accessed: 20-Feb-2017].

VITA

John Ciubuc started his Bachelors of Science in Biology at the University of Texas at El Paso in 2011. John Ciubuc joined the Peer-Led Team Learning (PLTL) in 2012, where he contributed both as a chemistry teacher assistant and chemistry workshop instructor. John Ciubuc completed his Bachelor of Science in Biology at the University of Texas at El Paso in 2014. He joined the Optical Spectroscopy and Microscopy Laboratory at the University of Texas at El Paso in 2015, where he pursued a Master's of Science in Biomedical Engineering. In Summer 2016, John Ciubuc was accepted in the Graduate Research Employment Program at the Mayo Clinic in Rochester Minnesota, where he collaborated together with the Neural Engineering Laboratory group at Mayo Clinic. During the development of this thesis, John Ciubuc also contributed to other research activities including fast-scan cyclic voltammetry, graphene for biomedical applications, ultrasensitive detection of neurotransmitters, and Raman computational and experimental studies of dopamine.

Contact Information: John.Ciubuc@gmail.com

This thesis was typed by John Ciubuc